REPORT DOCUMENTATION PAGE

Form Approved
OMB No. 0704-0188

PLEASE DO NOT RETURN YOUR FORM TO THE ABOVE ORGANIZATION.

1. REPORT DATE *(DD-MM-YYYY)*	2. REPORT TYPE	3. DATES COVERED *(From - To)*
15-12-2008	FINAL REPORT	1 MAR 2006-30 JUN 2008

4. TITLE AND SUBTITLE
Faraday Accelerator with Radio-frequency Assisted Discharge (FARAD)
A New Eletcrodeless Concept for Plasma Propulsion

5a. CONTRACT NUMBER

5b. GRANT NUMBER
FA9550-06-1-0149

5c. PROGRAM ELEMENT NUMBER

6. AUTHOR(S)
Prof. Edgar Choueiri

5d. PROJECT NUMBER

5e. TASK NUMBER

5f. WORK UNIT NUMBER

7. PERFORMING ORGANIZATION NAME(S) AND ADDRESS(ES)
Electric Propulsion and Plasma Dynamics Lab (EPPDyL)
Applied Physics Group
MAE Dept., Princeton University
Princeton NJ 08544

8. PERFORMING ORGANIZATION REPORT NUMBER

9. SPONSORING/MONITORING AGENCY NAME(S) AND ADDRESS(ES)
AFOSR/NA
875 N. RANDOLPH STREET STE 325
ARLINGTON, VA 22203

10. SPONSOR/MONITOR'S ACRONYM(S)
AFOSR

11. SPONSOR/MONITOR'S REPORT NUMBER(S)
(703) 696-7234

12. DISTRIBUTION/AVAILABILITY STATEMENT
Distribution A: Approved for Public Release

AFRL-SR-AR-TR-09-0011

13. SUPPLEMENTARY NOTES

14. ABSTRACT
A new electrodeless accelerator concept that relies on an RF-assisted discharge, an applied magnetic field, and electromagnetic acceleration using an inductive coil is presented. The primary advantage of this concept is that a preionized plasma is employed to lower the initial voltage threshold which applies to the formation of an inductive current sheet in other pulsed inductive accelerator concepts.

15. SUBJECT TERMS

16. SECURITY CLASSIFICATION OF:			17. LIMITATION OF ABSTRACT	18. NUMBER OF PAGES	19a. NAME OF RESPONSIBLE PERSON
a. REPORT	b. ABSTRACT	c. THIS PAGE			Edgar Choueiri
U	U	U	U	66	19b. TELEPHONE NUMBER *(Include area code)* (609) 258 5220

Faraday Accelerator with Radio-frequency Assisted Discharge (FARAD) A New Eletcrodeless Concept for Plasma Propulsion

FINAL REPORT
to the US Air Force Office of Scientific Research

GRANT NUMBER: FA9550-06-1-0149
October 2008

PI: Prof. Edgar Choueiri

Graduate Students: Kurt Polzin and Ashley Hallock

Electric Propulsion and Plasma Dynamics Lab (EPPDyL)
Applied Physics Group
MAE Dept., Princeton University
Princeton NJ 08544
Phone: (609) 258 5220 Fax: (609) 258 6875
E-mail: choueiri@princeton.edu

Contents

SYNOPSIS

A new electrodeless accelerator concept that relies on an RF-assisted discharge, an applied magnetic field, and electromagnetic acceleration using an inductive coil is presented. The primary advantage of this concept is that a preionized plasma is employed to lower the initial voltage threshold which applies to the formation of an inductive current sheet in other pulsed inductive accelerator concepts.

In the first chapter of this report we introduce the concept and describe its potential advantages. We then describe a proof-of-concept experiment, supported by optical and probe diagnostics, constructed and used to demonstrate low-voltage, low-energy current sheet formation and acceleration. Magnetic field data indicate that the peak sheet velocity in this unoptimized configuration operating at a pulse energy of 78.5 J is 12 km/s. Visual observations indicate that the plasma follows the applied magnetic field from the RF discharge to the face of the planar acceleration coil, while magnetic field probing and visualization using a fast-framing camera show the formation and acceleration of the current sheet. These observations and measurements provide the first proof of validity for the concept.

In Chapter 2, a model of the FARAD accelerator consisting of a set of coupled circuit equations and a one-dimensional momentum equation was nondimensionalized leading to the identification of several scaling parameters. Contour plots representing thruster performance (exhaust velocity and efficiency) were generated numerically as a function of the scaling parameters. The analysis and modeling allowed for obtaining a criterion that maximized thruster efficiency when the circuit's natural period was matched to the acceleration timescale. An additional insight was to show that a circuit with a highly underdamped current waveform leads to higher thruster performance.

In Chapter 3, the inductive formation of current sheets in a conical theta pinch FARAD is investigated experimentally with time-integrated photography. The goal is to help in understanding the mechanisms and conditions controlling the strength and extent of the current sheet in a conical pinch configuration, which are two indices important for FARAD as a propulsion concept. The profiles of these two indices along the inside walls of the conical acceleration coil are assumed to be related to the profiles of the strength and extent of the luminosity pattern derived from photographs of the discharge. The variations of these profiles as a function of uniform back-fill neutral pressure (with no background magnetic field and all parameters held constant) provided the first clues on the nature and qualitative dependencies of current sheet formation. It was found that there is an optimal pressure for which both indices reach a maximum and that the rate of change in these indices with pressure differs on either side of this optimal pressure. This allowed the inference that current sheet formation follows a Townsend-like breakdown mechanism modified by the existence of a finite pressure-dependent radio-frequency-generated electron density background. The observation that the effective location of the luminosity pattern favors the exit-half of the conical coil is explained as the result of the tendency of the inductive discharge circuit to operate near its minimal self-inductance. Movement of the peak in the luminousity pattern towards the upstream side of the cone with increasing pressure is believed to result from the need of the circuit to compensate for the increase in background plasma resistivity due to increasing pressure.

In light of the studies and findings reported in the first three chapters, a set of design rules aimed at producing a high-performance Faraday Accelerator with Rf-Assisted Discharge (FARAD) are presented in Chapter 4. The rules are discussed for optimization of each of the major processes in the FARAD: plasma acceleration, current sheet formation, applied field generation and mass injection and preionization. A combination of literature data, previous modeling results and physical intuition are employed to determine and justify the stated rules. A qualitative level of confidence is assigned to each statement based upon the supporting evidence employed to rationalize the rule. While some of the rules are complementary, further investigation and verification are required to determine if any directly conflict with each other.

Chapter 1

FARAD: Proof of Concept

Nomenclature

B - magnetic field [Gauss]; C - capacitance [F]; I, J - current [A]; j - current density [A m^{-2}]; L_0 - external inductance [H]; L_c - coil's inductance [H]; M - mutual inductance [H]; r - radial coordinate [m]; R_e - external resistance [Ω]; R_p - plasma resistance [Ω]; R_m - Magnetic Reynolds number; V_0 - initial voltage [V]; z - axial coordinate [m]; z_{emc} - electromagnetic coupling length scale [m]; ΔL - change in circuit inductance [H]; Δt_a - acceleration coil pulse length [s]; Δt_g - gas pulse length [s]; Δt_{RF} - RF pulse length [s]; μ - magnetic permeability [H m^{-1}]; ρ_0 - gas density [kg m^{-3}]

Additional subscripts

$_{\text{Applied}}$ - applied magnetic field component; $_{\text{Coil}}$ - acceleration coil component; $_r$ - radial component; $_z$ - axial component
$_\theta$ - azimuthal component

1.1 Introduction

Pulsed inductive plasma accelerators are spacecraft propulsion devices in which energy is stored in a capacitor and then discharged through an inductive coil. The device is electrodeless, inducing a current in a plasma located near the face of the coil. The propellant is accelerated and expelled at a high exhaust velocity ($\mathcal{O}$ (10 km/s)) through the interaction of the plasma current and the induced magnetic field.

Inductive plasma accelerators are attractive as propulsive devices for many reasons. The lifetime and contamination issues associated with electrode erosion in conventional pulsed plasma thrusters (PPTs) do not exist in devices where the discharge is inductively driven. In addition, a wider variety of propellants (e.g. CO_2, H_2O) becomes available for use when compatibility with metallic electrodes is no longer an issue. Moreover, pulsed inductive accelerators (indeed, pulsed accelerators in general)

can maintain the same performance level over a wide range of input power levels by adjusting the pulse rate.

We introduce a new pulsed inductive plasma accelerator concept, the **F**araday **A**ccelerator with **R**adio-frequency **A**ssisted **D**ischarge (FARAD). In this work we describe the results from a proof-of-concept experiment and not a working, optimized thruster. In the rest of this section we describe the FARAD concept and provide motivation for our research.

1.1.1 Description of the Concept

A schematic representation of the FARAD proof-of-concept experiment is shown in Fig. 1.1. In the schematic two joined cylindrical glass tubes form a vacuum chamber for the experiment. Plasma generation occurs in the smaller vessel while acceleration takes place in the larger-diameter, adjoining vessel. The chamber is surrounded by a set of applied B-field electromagnet coils, which are configured to produce a highly axial field inside the smaller tube and a highly diverging, mostly radial field near the flat back-end of the larger vessel, as shown by the representative applied B-field lines drawn in the figure.

In a FARAD thruster, gas is injected into the smaller tube (from the left in the picture) and is ionized by a helicon discharge, which requires the applied axial magnetic field and an RF/helicon antenna; the latter is shown wrapped around the outside of the smaller tube. A helicon discharge[1, 2, 3] is a radio-frequency inductive discharge that is very efficient as a plasma source. The highly ionized plasma is guided by the applied magnetic field to flow radially outward along the flat back-end of the adjoining larger vessel.

A flat inductive coil is mounted on the outer side of the back-end (which protects the coil from the plasma). The coil extends from the outer radius of the central opening to the inner radius of the larger vessel and is referred to as the acceleration stage. A large azimuthal current, labeled J_{Coil} in Fig. 1.1, is quickly pulsed through the coil. For a high-enough current rise rate[4], $dI/dt \geq 10^{10}$ A/s, this pulse induces a current sheet in the plasma, which initially forms parallel and very close to the back-end.

The current sheet, shown as a thin disk in the figure, contains an induced azimuthal current, labeled J_{Plasma}, which flows in the opposite direction to the current in the coil. The induced current density interacts with the magnetic fields resulting in a Lorentz body force density.

1.1.2 Motivation

The FARAD concept shares one main feature with a previous concept, namely the Pulsed Inductive Thruster (PIT)[5, 6, 7]. That feature is the inductive production and acceleration of a current sheet via a current pulse in an external coil. As such, we expect the propulsive characteristics of an optimized FARAD thruster to be quite comparable to the PIT ($I_{\mathrm{sp}} = 2000$-8000 s , $\eta_{\mathrm{t}} = 40$-50%).

The novelty of the FARAD is that the plasma is preionized by a mechanism separate from that used to form the current sheet and accelerate the gas. This is much different than that in the PIT where ionization, current sheet formation and acceleration are all

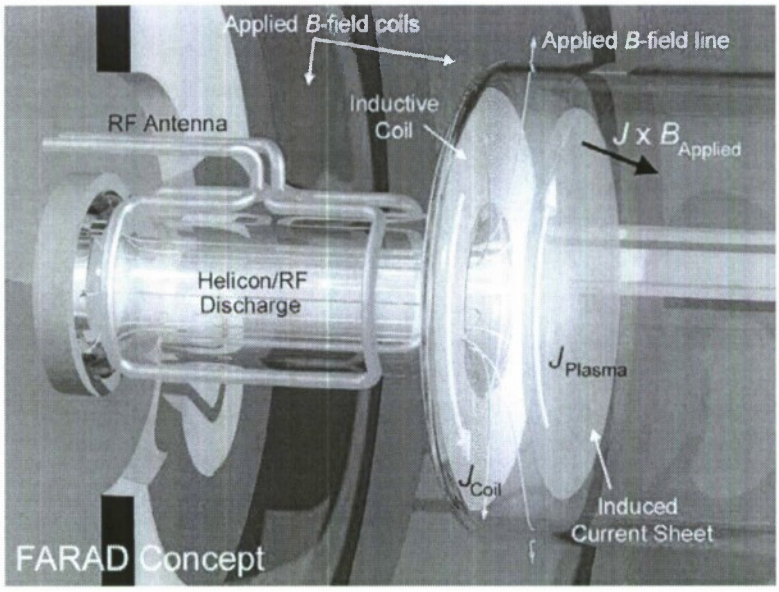

Figure 1.1: Schematic illustration of the FARAD concept.

performed by the pulse of current flowing through the acceleration coil. An additional conceptual difference is between the FARAD and the PIT is that in the FARAD the propellant is fed as a plasma from upstream of the acceleration stage instead of as a neutral gas fed from downstream by a sizeable nozzle.

We show in this chapter of the report that using a separate preionization mechanism, such as the one found in our experiment, allows for the formation of an inductive current sheet at much lower discharge energies and voltages than those used in the PIT, even though our proof-of-concept experiment is poorly optimized for inductive current sheet formation and acceleration. While the experimental data contained in this chapter were obtained at discharge energies of 78.5 J/pulse, inductive current sheets have been formed in the proof-of-concept experiment at energies as low as 44 J/pulse (versus 4 kJ/pulse in the PIT). Relief of the high energy, high initial voltage design constraint on pulsed inductive current sheet formation has the potential to lead to smaller, more compact thrusters for spacecraft systems.

In addition to the acceleration produced by the interaction of the induced magnetic field and plasma current, an additional acceleration component may be realized through the interaction of the applied magnetic field with the induced current. However, a strong applied magnetic field may impede the azimuthal current in the sheet, thus lowering thruster efficiency. Study of this aspect of the FARAD is beyond the scope of this chapter, but we mention it here as it merits separate investigation.

The outline for the rest of the chapter is as follows. In section 1.2 the FARAD proof-of-concept experiment is described while the diagnostics employed are briefly

described in section 1.3. Data demonstrating the concept of low voltage, low energy pulsed inductive acceleration are presented in section 1.4 and discussed in greater detail in section 1.5.

1.2 FARAD Proof-of-Concept Experiment

The different components of the FARAD proof-of-concept experiment are described below. These components are assembled to form the dedicated experimental facility shown in Fig. 1.2.

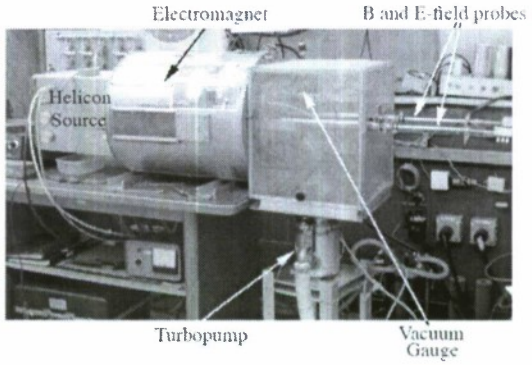

Figure 1.2: Photograph of the facility used for the FARAD proof-of-concept experiment. The picture shows the water-cooled electromagnet, Faraday cage, turbopump and associated equipment. The plasma helicon source is located inside the box on the left hand side.

1.2.1 Vacuum Vessel

The vacuum vessel consists of two Pyrex cylinders placed inside of an electromagnet. The small cylinder has a 6 cm inner diameter and is 37 cm in length while the large cylinder has a 20 cm inner diameter and is 46 cm in length. The cylinders are connected using a G-11 (fiberglass) plate with a 6 cm concentric hole at the center to allow free flow of gas between the two cylinders. A flat induction coil (used to accelerate the plasma) is mounted to the G-11 plate inside the vacuum chamber. A photograph of the small cylinder mated to the G-11 plate is shown in Fig. 1.3.

A constant background pressure (0.1 to 55 mTorr) can be maintained by a gas feed located at the endplate of the large cylinder and by a 150 l/s turbo pump with a conductance controller backed by a roughing pump. A background pressure of 5×10^{-6} Torr can be maintained while the turbo pump is operating and the conductance controller is in the open position.

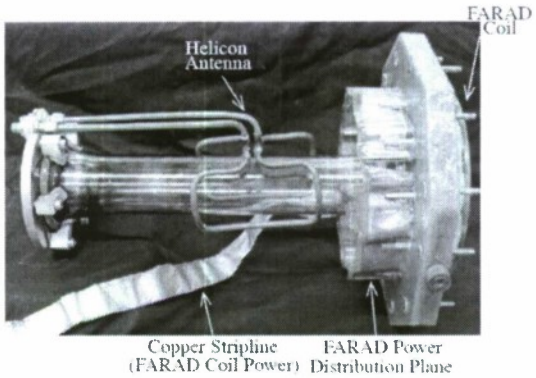

Figure 1.3: Side view of the fully assembled FARAD proof-of-concept experiment. This photograph can be compared directly to the conceptual schematic shown in Fig. 1.1.

1.2.2 Applied Magnetic Field

The applied magnetic field is generated using a Varian VA-1955A klystron magnet. (No effort at this proof-of-concept stage has been made to develop a compact magnet that would be more ideal for an actual thruster.) This apparatus contains five separate, water-cooled magnet coils (see schematic in Fig. 1.4). The magnet wiring has been altered to allow the currents in coils 1 and 2 and coils 3, 4 and 5 to be driven in opposite directions by two different power supplies. Using two Electronic Measurements EMCC 120-40 power supplies to drive the current in opposite directions in these coil sets, a cusped magnetic field can be created.

Magnetostatic Modeling

A 2-D axisymmetric numerical model of the magnet and case is constructed and solved using a magnetostatic modeling program (Maxwell SV, Ansoft Corp.). The model is shown to scale in Fig. 1.4. Each coil set consists of three separate, concentric, toroidal copper rings. Each ring carries an equal amount of the total assigned current. The magnet casing is modeled with a relative magnetic permeability of 60. As in the experiment, the currents in coil sets 1 and 2 flow in the same direction while coil sets 3, 4 and 5 are driven by a separate power supply in the opposite direction. Throughout this chapter, the axial position $z = 0$ is coincident with the location of the acceleration coil.

Applied Field Measurements

Measurements of the steady-state magnetic field in the coil were performed using an FW Bell gaussmeter (model 5080) calibrated to an accuracy of 1%. The axial and radial components of the field were measured on a grid with spacings in both the axial and radial directions of 1.27 cm (1/2"). This grid covers 10.16 cm (4") in the radial

direction and 58.42 cm (23") in the axial direction. The current provided by the power supply for coils 1 and 2 was 23.9 A while the current for coils 3, 4 and 5 was 10.2 A (e.g. total current assigned to coil set #1 = 23.9 A $\times$ 182 turns = 4350 A-turns). The results of the applied field measurement are given in the top half of Fig. 1.5 while the bottom half of the same figure shows results predicted by the magnetostatic model operating under the same conditions. The agreement with the model is excellent as the calculated and measured maps are practically indistinguishable.

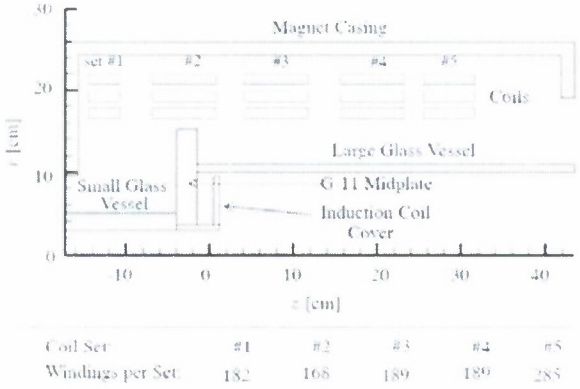

Figure 1.4: An axisymmetric schematic depicting the geometry of the magnet and vacuum vessel (to scale). The acceleration coil is located at $z = 0$ in all the plots in this chapter.

The magnetostatic model is used to find values for the current in each coil which would yield a mostly radial field at the coil face while still producing a mostly axial field in the helicon stage. For the given configuration, there are a wide range of current values for which an axial field is produced in the helicon stage. Plots of the magnetic field lines are used to identify field geometries which could deliver magnetized particles from the inductive discharge to the acceleration coil face. While a cusp magnetic field is produced in the proof-of-concept experiment, it is only an artifact of how the applied magnetic field is presently generated. Only the axial field in the helicon stage and the mostly radial field in the acceleration stage are truly necessary. In a real thruster, the radial field should have some finite value at the coil face and then drop quickly to near zero over a distance that is shorter than the acceleration length scale, helping to guarantee magnetic field detachment. Such a field geometry could be constructed using a combination of Helmholtz coils and magnetic pole pieces.

1.2.3 Plasma Generation

A Boswell-type saddle antenna (helicon antenna)[8] is placed around the small cylinder (shown on the left side of Fig. 1.3) and used to generate the plasma. The antenna is constructed of copper tubing to allow water cooling during operation. The heli-

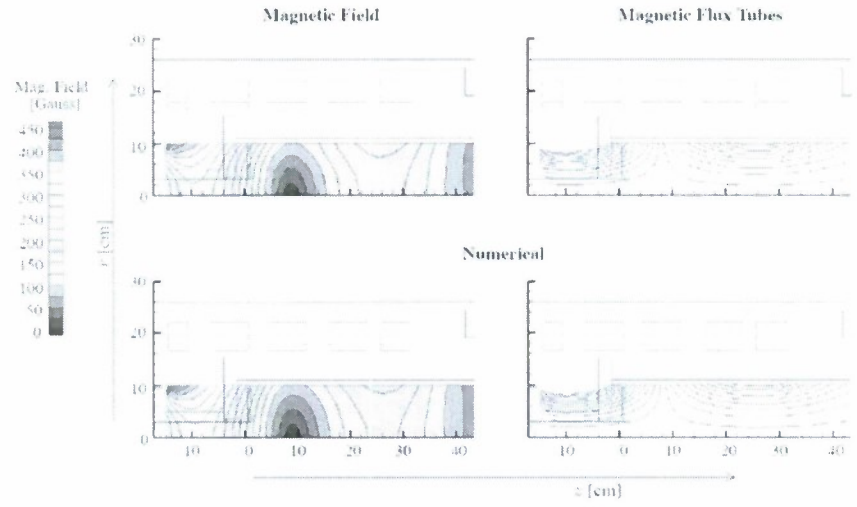

Figure 1.5: Applied magnetic field measurements (top) and modeling results (bottom) for the calibration case where the current in coils 1-2 is 23.9 A and the current in coils 3-5 is 10.2 A, showing excellent agreement.

con discharge[1, 2, 3] is produced by supplying power (steady-state or pulsed) to the antenna from an ENI 13.56 MHz, 1.2 kW power supply through a tuner. The tuner consists of an L network composed of two Jennings 1000 pF, 3 kV variable vacuum capacitors. It is located as close to the antenna as possible to maximize coupling efficiency.

At the power levels we operated the plasma source (500 W and above) the measured plasma density, electron density, electron temperature, reflected powers[9] as well as the luminous structure of the plasma inside the source (a bright pencil-like core of bright emission surrounded by a plasma) all correspond to what is commonly described as a helicon source in the literature (see Ref. [[2]] and the references within) as opposed to an inductive discharge. While the axial field strength in the small cylinder is approximately 400 Gauss for the data contained in this chapter, helicon discharges were ignited at field strengths of 175-200 Gauss.

1.2.4 Acceleration Coil

The FARAD acceleration coil (seen in Fig. 1.6) is similar to the Marx-type coil used by Lovberg and Dailey in later generations of the PIT[6]. However, it is quite different in scale and pulse energy. The PIT MkV coil is comprised of 18 half-turn coils, has an outer diameter of 1 meter and operates at roughly 4 kJ/pulse. The FARAD proof-of-concept experiment, on the other hand, possesses 12 half-turn coils, has an inner diameter of 20 cm and has been operated from 44 to 78.5 J/pulse.

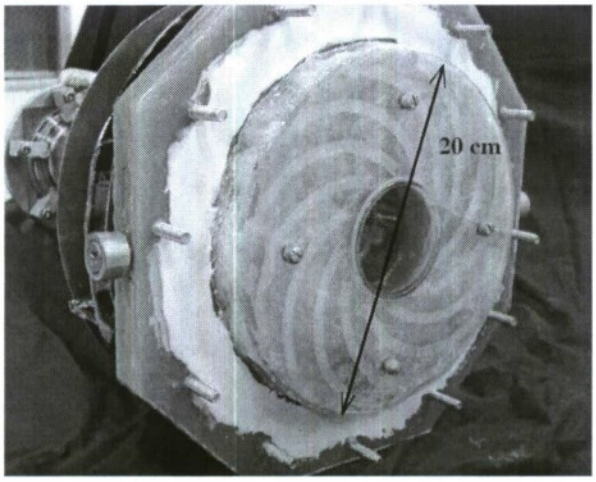

Figure 1.6: Skewed end view of the fully assembled FARAD experiment showing the face of the acceleration coil.

The half-turn coils are connected in parallel using copper strips. A 39.2 μF capacitor is remotely located and connected to the coil using copper stripline. Current is switched using a simple contact, or "hammer", switch. In a real thruster, SCRs or some other type of solid-state switching would be used. A lumped-element circuit schematic of the acceleration stage, showing both the driver circuit and the inductively coupled plasma, is shown in Fig. 1.7. The external circuit possesses capacitance C, external inductance L_0, resistance R_e, and acceleration coil's inductance L_C. The plasma also has an inductance equal to L_C and a resistance R_p. The two circuits are inductively coupled through the acceleration coil, which acts as a transformer with mutual inductance M.

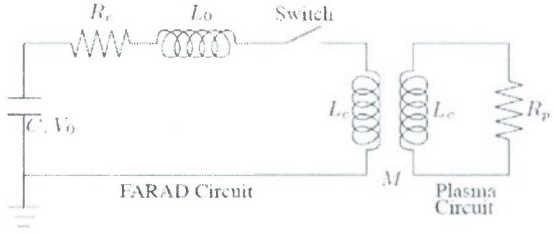

Figure 1.7: Circuit schematic of the FARAD acceleration coil and the inductively coupled plasma.

In a real thruster, one would want the fractional change in inductance to be high, ($\Delta L/L_0 > 1$). In our experiment, though, $\Delta L/L_0 \approx 15\%$. This is an unfortunate

effect of adopting the PIT's half-turn Marx-type coil geometry, which possesses a low inductance at small diameters. However, demonstrating current sheet formation and *any* subsequent acceleration in this unoptimized configuration serves to demonstrate the robustness of the concept. The coil's inductance can be increased in later generations of the FARAD by using multiple-turn spiral coils.

1.2.5 Experimental Operation

During operation of the FARAD proof-of-concept experiment, a helicon plasma is initiated and allowed to reach a steady-state condition. The duration of the helicon discharge prior to pulsing the acceleration coil is $\sim$ 1-2 secs. The helicon source remains active well after the acceleration pulse ($\mathcal{O}\,(1\text{-}10)\,\mu$s) is complete.

Thruster Pulsing Scheme

We note here that, in a real thruster, care should be taken in choosing the correct pulse widths and the inter-pulsing scheme. There are three major pulsed systems in the FARAD concept (the applied B-field being left in a steady-state mode for this discussion):

1. The neutral gas pulse, of temporal extent Δt_g, precedes the other pulses and should be long enough to fill the helicon stage with neutral gas but short enough to avoid leaking gas to the second (acceleration) stage.

2. The RF pulse length, Δt_{RF}, is the duration that power is supplied to the helicon stage. While the helicon stage can be operated in a steady-state mode (as we have done in the proof-of-concept experiment), it must be operated in a pulsed mode in a real thruster since the acceleration mechanism itself is pulse. In a real thruster the RF pulse is not started until the injected gas has filled the helicon stage and must end late enough to allow most of the produced plasma to migrate to the back-end of the acceleration stage but early enough to avoid producing extraneous plasma that may not participate in the acceleration process.

3. The acceleration coil pulse, Δt_a, must not start until most of the plasma has been guided to the back-end of the acceleration stage and must not end until the current sheet has traveled an axial distance z_{emc}, which represents the axial extent of the region (measured from the back-end) in which electromagnetic coupling between the sheet and the coil occurs. For axial locations $z \geq z_{emc}$ the current sheet is decoupled from the acceleration coil.

The demand for a fast gas valve can be alleviated by employing a burst-pulse scheme similar to that developed for gas-fed pulsed plasma thrusters[10, 11]. In this mode, a "slow" and sturdy valve is operated at a low duty cycle and the thruster is operated in a burst of discharge pulses, with a Δt between each consecutive *pulse* equal to the time it takes the current sheet to sweep the gas through the thruster. The time between the *bursts* is dictated by the available steady-state power and the required (average) thrust. If the response time of the RF-matching network is too slow to switch the

preionization pulse on and off for each individual acceleration pulse, it too can operate at the lower duty cycle associated with the "slow" valve.

Optimization of the pulsed systems is beyond the scope of the proof-of-concept experiment since an ambient fill technique and steady-state RF discharge were used. However, it is clear that the pulse inter-sequencing and relative magnitudes of Δt_g, Δt_{RF} and Δt_a will have significant impact on both the mass utilization efficiency and the propulsive performance of a real thruster and require further investigation.

1.3 Diagnostics

1.3.1 Current Monitoring

The current flowing through the acceleration coil, J_{Coil}, is monitored using an air-core Rogowski coil[12]. The raw probe output, which is proportional to the derivative of the enclosed current, is integrated numerically to yield a current waveform. The error on the calibration constant, which multiplies the integrated Rogowski coil waveform, is $\pm 3\%$ and the numerical integration errors have been estimated to add an additional 2% error for a total of $\pm 5\%$

1.3.2 Induced Magnetic Field

The induced (time-varying) magnetic field measurements are acquired using B-dot probes[13]. Three Panasonic 220 nH wire-wound non-magnetic core surface mount inductors are used to measure dB/dt in three orthogonal direction. The probe head is contained within a glass tube which protects it from the plasma. The tube diameter is on the order of mm, so as to not significantly disturb the plasma. The numerically integrated dB/dt signals are multiplied by their respective calibration constants and linearly combined to obtain $B(t)$ in the r-θ-z coordinate system. The error on the measurement of B_r is $\pm 5\%$. The radial location for our measurements is given schematically in Fig. 1.8.

1.3.3 Current Sheet Visualization

Visualization of current sheet formation and its subsequent motion is accomplished using a Hadland Photonics Imacon 792/LC fast-framing camera. The photographs are obtained using a 20 million frames per second module, with each frame having an exposure time of 10 ns. Due to obstructions in the optical path, only one region of the plasma, located on the face of the acceleration coil and extending 20 mm in the vertical direction, is imaged. A mask is affixed to the outside of the vacuum vessel to allow the current sheet's absolute position to be determined in each exposure. Consequently, the imaging plane is located at the edge of the vacuum vessel to properly image the mask (see Fig. 1.8 for the relative location of the imaging plane). The photographs are obtained without filtering, so any light emission that is bright enough to be imaged is seen. However, the RF/helicon plasma that reaches the acceleration coil face did not

produce enough light on its own to appear in any of our photographs, so we assume that the light captured in each exposure corresponds to emission from the current sheet.

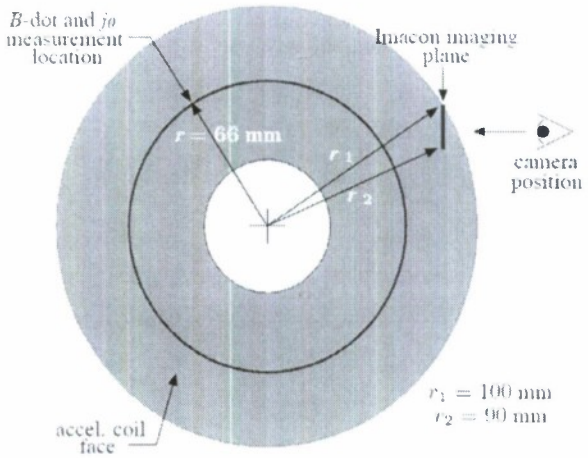

Figure 1.8: A schematic showing the relative locations of 1) the magnetic field probe data and 2) the plane imaged by the fast-framing Imacon camera. The schematic is to scale, and the vertical extent of the imaging plane matches the extent of the images presented in this chapter.

1.4 Experimental Data

In this section, data is presented which demonstrates the formation of a low-energy, low-voltage current sheet. In addition, the sheet experiences significant acceleration during the first half-cycle of the discharge. The working gas for these data is argon at 23 mTorr (in both the helicon and acceleration stages). The chamber is first evacuated and then a uniform fill technique is used to introduce the gas. The pressure is chosen because the strongest current sheet (determined using magnetic field traces, fast-framing photography, and naked-eye observations) forms at this pressure. The helicon is operated at 1000 W of forward power, but operation down to 500 W result in insignificant changes in the magnetic field waveforms and photographic images.

1.4.1 Visual Observations

Simple visual observations provided verification of the passive magnetic-field-guided plasma injection onto the acceleration coil face. The helicon plasma is quite luminescent and can be seen following the applied magnetic field lines and spreading over the acceleration coil (see Fig. 1.9). The luminosity is greatest at the centerline of the device and decreases with increasing radius. This is not surprising since we expect that the

initial, preionized plasma density scales like $1/r$ as the plasma spreads radially outward across the accelerator coil face. In the current configuration, a great deal of the plasma stays anchored alone the centerline and is not turned. This issue would have to be addressed in a real thruster. Also, the plasma density in a real thruster, while being greatest near the centerline, must be of a sufficient magnitude at the outside edge of the coil to allow for low voltage current sheet to form over the entire coil face.

Visual observations provide evidence of current sheet formation. When current is pulsed through the acceleration coil, a very bright 'flash' of light appears in a thin region near the coil. The flash appears homogeneous over the face of the coil and its intensity temporarily overwhelms the light emitted by the steady-state (helicon) plasma. The short duration, bright light emission is indicative of increased ionization due to current sheet formation across the coil face. While these observations are only qualitative, it is important to note that no current sheet formation was observed when the preionized plasma was not present. This leads to the conclusion that our configuration directed 'enough' preionized plasma to the acceleration coil face to allow for the formation of a current sheet at low discharge energies.

Figure 1.9: Photograph of the steady-state RF plasma as it follows magnetic field lines and spreads out over the face of the acceleration coil (viewed through a 1.0 neutral density filter). The bright area adjacent to the back-end, where the acceleration coil is located, is emission from the injected plasma. The grid pattern in the picture is due to the mesh of the Faraday cage enclosing the experiment and the dark, rectangular shape near the centerline is a structural member outside the chamber.

1.4.2 Coil Current

A typical driver circuit current waveform is given in Fig. 1.10. Since the fractional change in the inductance is low, the coil current is roughly the same with or without a current sheet present. The maximum dI_{Coil}/dt in our circuit is roughly 1.8×10^{10} A/s, which is on the order of the level required to form a current sheet[4].

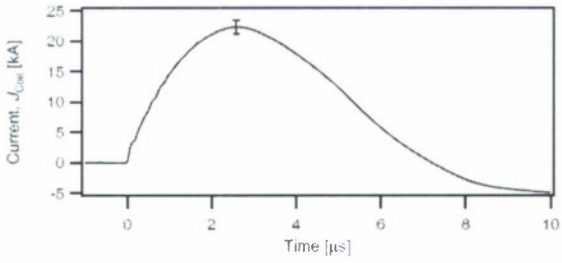

Figure 1.10: Total current in the aeceleration coil, J_{Coil}, (with a typieal error bar) for a pulse energy of 78.5 J.

1.4.3 Magnetic Field

Applied Field

Values of the applied (steady-state) magnctic field are computed numerically using the magnetostatic model presented in section 1.2.2. For completeness, plots of the variation of the applied field (B_r and B_z) along an axial linc at a radius of 66 mm arc given in Fig. 1.11. In the model, coils 1-2 are supplied with 38 A while 36.5 A are delivered to coils 3-5 by the power supply. These currents match those used during the experimental trials. The B_r field peaks just in front of the coil while the B_z field at that location goes to zero, as expected.

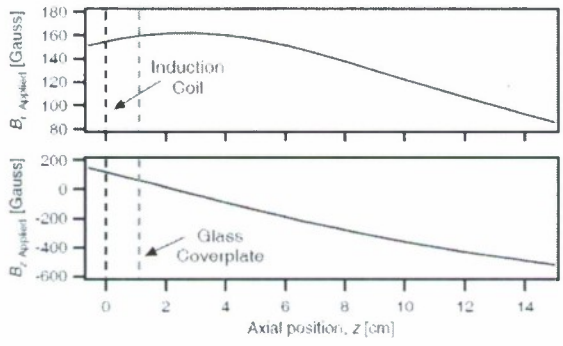

Figure 1.11: Calculated applied magnetie field strengths in the r and z direetions in front of the accleration coil at a radius of 66 mm. The coil position ($z = 0$) and the location of the surface of the glass plate covering the coil are sketched in the plot.

The magnitude of the applied field and a rough measure of the number density at the coil face before the pulse (found as 10^{11} cm^{-3} using an RF-compensated Langmuir probe) ean be used to compute the electron and ion Hall parameters and the collisional mean free paths in the experiment before the pulse. The calculations reveal that the

electrons are partially magnetized ($\omega_{ce}/\nu_{ei} \gg 1$, electron-neutral mean free path on the order of centimeters) but the ions are not ($\omega_{ci}/\nu_{ii} \ll 1$). (Note that some ions may be turned by microscopic polarization fields forming as the more mobile electrons turn along the field lines and race towards the outer edge of the acceleration coil.) While this is acceptable for our proof-of-concept experiment, the ions in a real thruster would have to be turned by either a much stronger applied field or some type of duct or nozzle to avoid a low mass utilization efficiency.

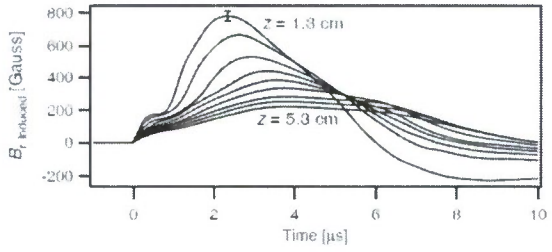

Figure 1.12: Time histories of the induced radial magnetic field strengths (with a typical error bar) at various axial stations at a radius of 66 mm. The axial positions are spaced evenly every 5 mm. The discharge energy was 78.5 J and the background pressure was 23 mTorr.

Induced Field

Data showing the temporal and spatial variation of the induced radial field acquired at a radius of 66 mm are presented in Fig. 1.12. The axial, z, locations are evenly spaced every 5 mm between 1.3 cm and 5.3 cm from the coil face. We see first that the induced field strength is stronger than the applied magnetic field, temporarily overwhelming the latter's effect on the plasma during the pulse. Notice that the traces all begin increasing immediately at $t = 0$. This feature has been previously observed in pulsed inductive devices[5, 14] and indicates that the initial fields induced by the coil rapidly diffuse through the plasma, implying low initial conductivity. At a time shortly after $t = 0$, the waveforms exhibit a distinct 'knee', or inflection point. This 'knee' is indicative of current sheet formation and the associated increases in plasma conductivity and electromagnetic shielding that accompany it. The field emanating from the current sheet propagates at the speed of light through the weakly ionized downstream portion of the plasma causing all the 'knees' to appear coincident (or very nearly so) in time.

Current Density

Magnetic field maps, like those presented in Fig. 1.12, provide a good qualitative indication of the presence and effect of a current sheet. However, as the induced magnetic field is a linear superposition of two separate current sources, the current in the coil

and the induced current sheet there is a great deal of ambiguity involved in the interpretation of field data acquired along a single, axial line. This difficulty is bypassed by measuring the magnetic field in a two-dimensional r-z plane and using Ampère's law,

$$\nabla \times \mathbf{B} = \mu_0 \mathbf{j},$$

to compute the current density, j_θ, in the sheet. This works because the only portion of the magnetic field in the region of interest that is not curl-free is attributable to the current sheet.

Azimuthal current density profiles in the FARAD experiment are presented in Fig. 1.13. To numerically compute the curl of B, data on a two-dimensional, r-z grid are required. The axial spacing, Δz, between the magnetic field data points is 5 mm and the radial spacing, Δr, is 4 mm straddles $r = 66$ mm. The error bars are a combination of the errors on the magnetic field measurements and the uncertainty on the B-dot probe positions.

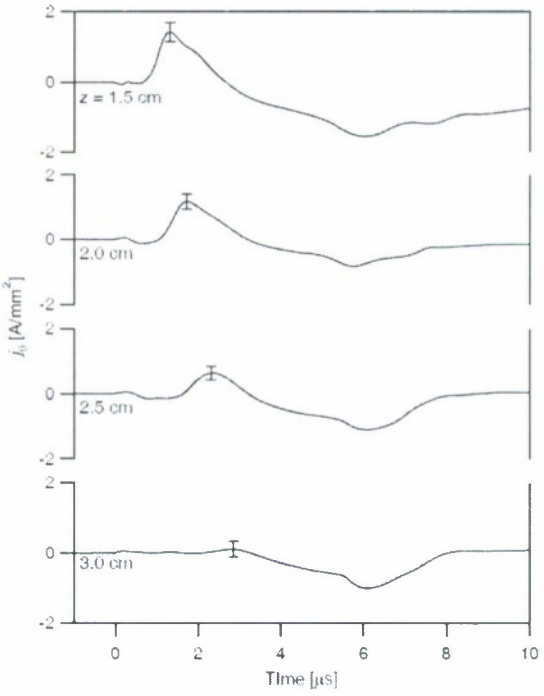

Figure 1.13: Time histories of the induced plasma current densities (with typical error bars) at various axial stations at a radius of 66 mm. The axial positions are spaced evenly every 5 mm. The discharge energy was 78.5 J and the background pressure was 23 mTorr.

The initial peak in the current density profile at each axial station represents the

current sheet. We observe a weakening of the sheet as it reaches axial stations located further away from the acceleration coil. The current sheet velocity can be estimated based upon the time the peak current passes the different axial stations. The inferred current sheet velocity between $z = 1.5$ cm and $z = 2.0$ cm is 12 km/s, while the velocity between $z = 2.0$ cm and $z = 2.5$ cm is 8 km/s.

The induced current in the plasma goes to zero when the current in the external circuit is maximum (see Fig. 1.10). Also, the azimuthal current at every displayed axial station turns negative once the coil current passes through its maximum, i.e. when dJ_{Coil}/dt changes sign producing a weak induced azimuthal current throughout the entire volume. We conclude that the formation of an inductive current sheet must possess some minimum threshold dJ_{Coil}/dt value and in our experiment this threshold is not attained when the external current pulse reverses.

1.4.4 Current Sheet Visualization

A track of the current sheet position is presented in Fig. 1.14 while representative photographs of the current sheet at several instances in time are presented in Fig. 1.15. The current sheet locations found in Fig. 1.14 are determined as follows. Digitized frames are loaded into a program capable of performing image processing operations (Igor Pro, Wavemetrics Inc.). The intensity values of individual pixels are summed in the vertical, r, direction yielding a waveform comprised of summed intensity as a function of z. A Gaussian distribution is then fit to the intensity waveform,

$$\text{Intensity} = A \exp\left[-\left(\frac{z - z_0}{\sqrt{2}\sigma}\right)^2\right],$$

where A is a constant, z_0 is taken to be the current sheet center and σ is taken as a measure of the error on z_0.

The track (Fig. 1.14) clearly shows three separate phases in the discharge; initiation, acceleration, and termination. The images presented in Fig. 1.15 are meant to be representative of the discharge and will aid in our interpretation of the photographic data. (Note that while the images in Fig. 1.15 were contrast enhanced, the raw images analyzed in the production of Fig. 1.14 were not enhanced.) The current sheet initiates at $z = 18.4$ mm and remains stationary, with its light emission increasing and intensifying until $t \approx 1.1$ μs. It then quickly accelerates, reaching a constant velocity which it maintains between 1.1 and 2.4 μs. A linear curve fit of this portion of the data yields a sheet speed of approximately 4.6 km/s. Finally, between 2.4 and 3 μs, the current sheet's motion ceases and its light emission decreases. The termination phase occurs as dJ_{Coil}/dt in the external circuit approaches zero, mirroring the result of the current density measurement.

1.5 Discussion

Our measurements clearly indicate that the preionized plasma couples with the current in the acceleration coil to further ionize the gas and form a current sheet. The delay

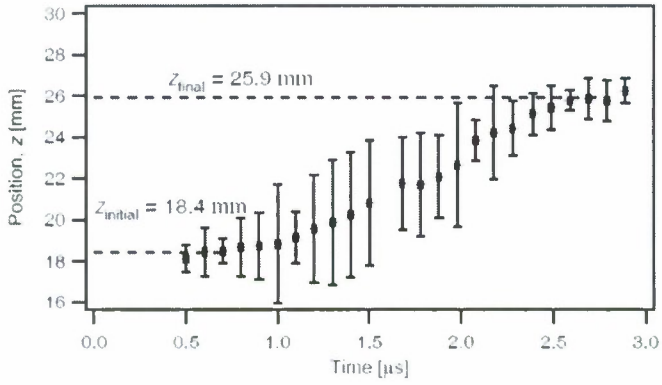

Figure 1.14: Current sheet position history obtained using the fast-framing camera. Error bars show the width of the Gaussian fit to the luminous portion of the discharge. The discharge energy was 78.5 J and the background pressure was 23 mTorr.

between when the coil current is pulsed and when the current sheet forms poses a serious efficiency problem for a real pulsed inductive accelerator as magnetic field energy, which could perform work, is instead radiated into free space. While we encounter this problem in our proof-of-concept experiment, we expect that increasing the initial current rise rate in the coil, which can be done by lowering the parasitic inductance L_0, will help in minimizing the time between pulse initiation and current sheet formation as it did in Ref. [[5]].

The measurements of the induced magnetic field and azimuthal current density (referred to as the field measurements throughout this discussion) compare quite well with the current sheet visualization and analysis (referred to hereafter as the optical measurements). Both measurements indicate that, after an initial delay, a current sheet forms and moves a finite distance. Since the coil's inductance, and consequently the mutual inductance, M, between the coil and the sheet, are relatively small in the experiment, the plasma sheet dynamics are effectively driven only by dJ_{Coil}/dt. Consequently, the sheet terminates as dJ_{Coil}/dt approaches zero. Increasing the coil inductance in a real thruster will result in a current sheet with longer lifetime that also experiences additional acceleration (both processes are driven by dJ_{Coil}/dt and dM/dt).

There are, however, two apparent discrepancies between the field and optical measurements. Examination of these apparent discrepancies leads to additional physical insight into the current sheet evolution.

The first discrepancy is the difference between the sheet velocity (12 km/s) obtained from the magnetic field probe data and that (4.6 km/s) inferred from the photographs in Fig. 1.15. This discrepancy may be qualitatively explained in light of the observed induced magnetic field gradient, $\partial B_r/\partial r$, which implies a weakening of the induced magnetic field, and thus a lowering of the sheet velocity, at the outer radial location

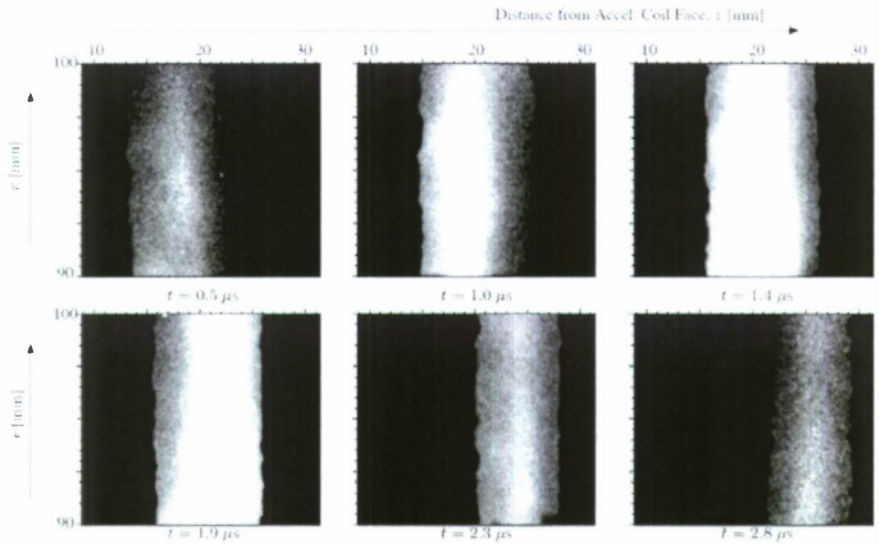

Figure 1.15: Representative high-speed photographs acquired using a fast-framing camera at a framing rate of 20 million frames per second. These photos show the sheet initiation ($t = 0.5$ μs), acceleration ($t = 1.0$ μs to $t = 2.3$ μs) and termination ($t = 2.8$ μs). (The contrast in these photographs has been enhanced through digital image processing.)

(90-100 mm) where the photographic observations were obtained, as compared to the radial location ($r = 66$ mm) where the magnetic probe measurements were made.

The second discrepancy is the difference between the axial positions of the current sheet when determined optically and from the probe data at a given time. For instance, at $t \approx 1.4$ μs, the sheet axial position is observed optically to be at about $z \approx 20$ mm from the backplate (Fig. 1.15) while the probe data (Fig. 1.13) give $z \approx 15$ mm. This can be explained by first noting from Fig. 1.11 that the applied magnetic field lines in the acceleration stage are not purely radial but are in fact tilted by about 20 degrees with respect to the backplate. This canting of the applied magnetic field should be expected to lead to a canted current sheet when the latter is initially formed. It is therefore not surprising that the initial axial position of the sheet at outer radii (where the optical measurements were made) leads the axial location of the sheet at inner radii (where the probe is located). The radially decreasing axial sheet velocity discussed in the previous paragraph compensates somewhat for this initial canting as the sheet evolves in time.

Triple probe measurements were unsuccessfully attempted in this experiment. We believe these measurements were unsuccessful for two reasons. The first is that no power supply with a fast enough response time was available for use in our experiment. The second is that many of the assumptions made in Langmuir and triple probe theory (specifically that the plasma is non-magnetized and the sheath is collisionless) are vi-

olated during the discharge pulse. Using the laser interferometry system described in Ref. [[15]] we were able to measure the maximum plasma density as roughly 7×10^{14} cm^{-3}. However, this density is at the very edge of the system's resolution, so no further, time-resolved measurements could be attained.

One may wonder if the current sheet is actually accelerating any mass. Since no thrust stand measurements were performed, this is a valid concern. If the entire fill density was accelerated by the $\mathbf{j} \times \mathbf{B}$ body force ($j_\theta = \mathcal{O}(1\ \mathrm{MA/m^2})$, $B_\mathrm{r} = 0.06\ \mathrm{T}$, $\rho_0 = 5 \times 10^{-5}\ \mathrm{kg/m^3}$, $t = \mathcal{O}(1\ \mu\mathrm{s})$) it would only reach a speed on the order of 1 km/s. However, this assumes that the sheet perfectly entrains all the mass available to it. Research in pulsed plasma thrusters has shown that the current sheet is, in fact, permeable and a certain amount of gas can slip behind the sheet[16]. One way to infer whether mass is accelerated is to compute the electron-ion momentum exchange coulomb mean free path. If we take $n_e = \mathcal{O}(10^{14}\ \mathrm{cm}^{-3})$ and $T_e = 2.5$ eV, then the mean free path is 1-2 mm, implying significant momentum coupling between the electron and ion fluids on the length scale of the observed motion. Moreover, the luminous front, which can only be emission from excited argon ion states, is not merely the result of an ionization front going through the gas, but a manifestation of a current sheet entraining at least some ions that are coupled to the electrons by momentum exchange collisions (which on a macroscopic scale is equivalent to a neutral plasma gaining acceleration via a $\mathbf{j} \times \mathbf{B}$ body force).

1.6 Conclusions

We have presented a new RF-assisted pulsed inductive accelerator concept, FARAD, and presented the results from a proof-of-concept experiment aimed at demonstrating the principle of low-energy, low-voltage inductive current sheet formation. The following conclusions can be made:

- Partially decoupling the ionization and acceleration processes through the use of a separate preionization mechanism in the FARAD allowed for current sheet formation at substantially lower discharge voltages and energies than previous pulsed inductive accelerator concepts (44 J/pulse as opposed to 4 kJ/pulse in the PIT).
- Visual observations in the proof-of-concept experiment indicate that pre-ionized plasma follows magnetic field lines and forms a plasma slab on the face of the acceleration coil. Also, when current is pulsed through the acceleration coil, a bright flash on the coil surface is visible to the naked eye, indicative of increased ionization associated with current sheet formation.
- Magnetic field probing gives qualitative evidence of the presence and effect of a current sheet. The curl of the induced magnetic field yields a direct measure of the current density profile at different axial stations within the acceleration stage. A peak sheet speed of 12 km/s is inferred from that data.
- Visualization using a fast-framing camera provides an observation of the formation of the current sheet and its subsequent acceleration.

- There are discrepancies in the sheet speed inferred from the magnetic field measurements and that found using photography (though both inferred speeds are of the same order). However, these discrepancies should be expected since the magnetic field probing and photographic measurements are obtained at different radial locations possessing different induced field strengths.
- Due to the finite axial component of the applied magnetic field in the acceleration stage, the current sheet, which forms at the location of the preionized plasma following the applied field lines, is initially canted forward at larger radii. This canting is alleviated as the sheet accelerates to higher velocities at lower radii due to an induced magnetic field which decreases with increasing radius.

Chapter 2

Non-dimensional Acceleration Model for FARAD

2.1 Introduction

There exists a one-dimensional pulsed inductive acceleration model similar to the type used in PPT analysis[17, 6]. This model differs from its PPT counterpart in that it must account for a second, inductively coupled circuit in the circuit equations. Unfortunately, since there has not been work analogous to the PPT research in deriving and interpreting physically meaningful parameters, designs of pulsed inductive accelerators are currently being performed using a set of empirical rules found to work over the years. The purpose of the study documented in this chapter is to identify nondimensional scaling parameters that control accelerator performance (exhaust velocity and thrust efficiency). When possible, we shall attempt to use the corresponding PPT nondimensional parameters to aid in the physical interpretation of the inductive acceleration terms.

The outline for the rest of this chapter is as follows. In Section 2.2, the dimensional equations governing the operation of a pulsed inductive accelerator are first presented and then nondimensionalized to yield the relevant scaling parameters. In the following section, the physical meanings of the various scaling parameters are distilled using both an understanding gained from past PPT research and some limiting-case solutions to the nondimensional equation set. In Section 2.4, performance of a pulsed inductive accelerator is computed by solving the full nondimensional equation set as a function of the nondimensional parameters. Contours of constant accelerator performance are plotted and specific features and trends in the data as a function of the various scaling parameters are interpreted based upon the physical insight gained in the previous section. The computed performance contours lead to additional physical insights into the acceleration process which are discussed in Section 2.5.

2.2 Governing Equations

2.2.1 Dimensional Equation Set

The equations governing the operation of a pulsed inductive accelerator have been previously derived by Lovberg and Dailey[17]. In this work, we shall briefly review the equation set and refer the reader to the earlier work for more detailed derivations of the equations.

Circuit Equations

A lumped-element circuit model of a pulsed inductive accelerator is presented in Fig. 2.1A. This model applies to both the PIT and FARAD variants of a pulsed inductive accelerator. The external circuit (left side of the figure) possesses capacitance C, external inductance L_0, resistance R_e, and acceleration coil inductance L_C. The plasma also has an inductance equal to L_C and a resistance R_p. The two circuits are inductively coupled through the acceleration coil, which acts as a transformer with mutual inductance M. The value of M is a function of the current sheet position z.

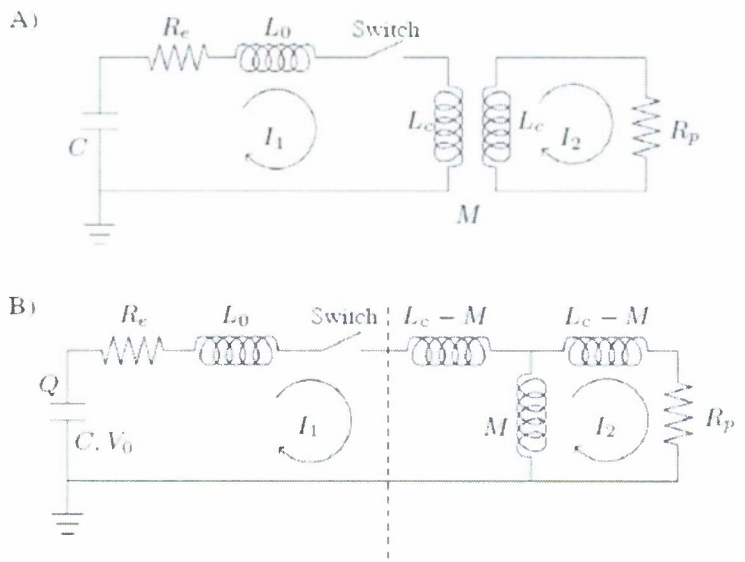

Figure 2.1: A) General lumped element circuit model of a pulsed inductive accelerator. B) Equivalent electrical circuit model. (After Ref. [17])

The circuit drawn in Fig. 2.1A is redrawn as an equivalent circuit in Fig. 2.1B. A set of circuit equations are written through the application of Kirchoff's law to each loop. Rearranging the equations and adding a statement for the time-rate of change of

charge on the capacitor, the following coupled set of first-order ordinary differential equations is obtained:

$$\begin{aligned}
\frac{dI_1}{dt} &= \frac{VL_C + (MI_1 + I_2L_C)\frac{dM}{dt} - I_2MR_p - I_1R_eL_C}{L_C(L_0 + L_C) - M^2}, \\
\frac{dI_2}{dt} &= \frac{M\frac{dI_1}{dt} + I_1\frac{dM}{dt} - I_2R_p}{L_C}, \\
\frac{dV}{dt} &= -\frac{I_1}{C},
\end{aligned} \tag{2.1}$$

where V is the voltage on the capacitor.

In a pulsed inductive accelerator, the circuit inductance changes through the value of the time changing mutual inductance term, $M(z(t))$. The inductance downstream of L_0 and R_e (i.e. to the right of the dashed line in Fig. 2.1B), referred to as the coil terminal inductance, can be written as

$$L_{term} = (L_C - M) + \frac{1}{(1/(L_C - M)) + (1/M)},$$

which after some algebraic manipulation becomes

$$L_{term} = L_C - \frac{M^2}{L_C}. \tag{2.2}$$

The inductance of a planar, spiral inductive coil coupled to a plasma current sheet is difficult to compute analytically. However, based on experimental measurements, it has been found[17] that the inductance can be modeled using the simple exponential function

$$L_{tot}(z) = L_0 + L_C(1 - \exp(-z/z_0)), \tag{2.3}$$

where z_0 is defined as the decoupling length. Using Eqs. (2.2) and (2.3) we arrive at a solution for M as

$$M = L_C \exp\left(-\frac{z}{2z_0}\right), \tag{2.4}$$

which, when differentiated results in the following equation that governs the changing mutual inductance of the circuit:

$$\frac{dM}{dt} = -\frac{L_C}{2z_0}\exp\left(-\frac{z}{2z_0}\right)\frac{dz}{dt}. \tag{2.5}$$

Momentum Equation

As the current sheet moves forward, it entrains and accelerates any gas that it encounters. The propellant mass in the current sheet as a function of time can be written as

$$m(t) = m_0 + \int_{t=0}^{t} \rho_A v_z \, dt, \tag{2.6}$$

where $\rho_A = \rho_A(z(t))$ is the linear mass density distribution and v_z is the sheet velocity. The term m_0 represents the initial mass of propellant in the sheet while the integral term represents the mass accumulated by the sheet as it moves away from the acceleration coil.

The momentum equation for this system can be written as

$$\frac{L_C I_1^2}{2 z_0} \exp(-z/z_0) = \rho_A v_z^2 + m(t) \frac{dv_z}{dt}. \tag{2.7}$$

The left hand side represents the self-field electromagnetic force generated through the interaction of the current and the magnetic field. The first term on the right hand side in Eq. (2.7) is the momentum investment associated with 'snowplowing' propellant (i.e. accelerating the newly entrained propellant encountered by the sheet from rest to the sheet speed) while the second term involves further acceleration of the already entrained propellant.

Plasma Model

In general, a model of the plasma is required to close the set of equations. This would typically yield a value for the plasma resistance, R_p, found in Eq. (2.1). A full treatment of this problem is quite complex and requires the use of complex MHD codes that incorporate self-consistent treatments of the non-equilibrium physical phenomena such as radiation, ionization, recombination, Joule heating and acceleration. Such detailed modeling is beyond the scope of the present study and the reader is referred to the ongoing work that aims to perform exactly this type of detailed multidimensional modeling of pulsed inductive plasmas[18]-[19].

In previous studies[6] using the simplified, one-dimensional model described in this section, the energy equation was eliminated by the explicit assumption of an electron temperature with the underlying implicit assumptions of local thermodynamic equilibrium and the ideal gas equation of state. These assumptions allow for an approximate computation of the plasma resistance, R_p. While not strictly self-consistent with the rest of the approach, the assumption of a constant electron temperature can be justified to a certain extent when dealing with elements like argon, which possess many levels of excitation and ionization that tend to 'thermostat' the electron temperature to a narrow range over a large span of currents and number densities[17].

We should mention here before moving on that there are a number of other implicit assumptions which have been made in the derivation of the acceleration model. The most important one is that current sheet formation is both immediate (at $t = 0$) and complete (does not allow the induced magnetic field to diffuse through it). This assumption has proved most difficult to achieve experimentally.

2.2.2 Nondimensional Equations

Following Ziemer and Choueiri's modeling of a PPT[20], we nondimensionalize the inductive accelerator's set of governing equations in an attempt to identify relevant scaling parameters and find their optimum values. However, differences between the models for these two accelerators arise due to the following:

1. In the inductive thruster acceleration there are two dependent current loops while there is only the one loop in PPTs.

2. The mutual inductance term also does not appear in PPT modeling; however it is essential to the coupling between the two current loops in an inductive accelerator.

We also recall that the inductive acceleration model we are employing lacks a model of the plasma. The issue of incorporating a model of the plasma can be sidestepped by finding non-dimensional scaling parameters and searching for physical insight instead of attempting to exactly model an accelerator. To determine the sensitivity of the acceleration process to the plasma resistance we could simply vary any dimensionless parameter which contains R_p.

The following dimensionless terms can be readily selected as a starting point based upon prior knowledge of PPT scaling laws:

$$\begin{aligned} t^* &= \frac{t}{\sqrt{L_0 C}}, \\ I_1^* &= \frac{1}{V_0}\sqrt{\frac{L_0}{C}}\, I_1, \\ I_2^* &= \frac{1}{V_0}\sqrt{\frac{L_0}{C}}\, I_2. \end{aligned} \tag{2.8}$$

In the course of nondimensionalizing the governing equations the following additional nondimensional variables naturally appear in the equation set:

$$\begin{aligned} z^* &= \frac{z}{z_0}, \\ V^* &= \frac{V}{V_0}, \\ M^* &= \frac{M}{L_C}, \\ v_z^* &= \frac{\sqrt{L_0 C}}{z_0}\, v_z. \end{aligned} \tag{2.9}$$

In the framework of Eq. (2.6), the propellant can either be loaded as a slug mass ($\rho_A = 0$ for all z) or as some function of position ($\rho_A = \rho_0\, f(z)$). If the propellant is loaded as a slug mass and we nondimensionalize by the propellant mass per shot, m_{bit}, the non-dimensional mass accumulation statement can be written as

$$m^* = \frac{m(t)}{m_{\text{bit}}} = 1 \quad \text{for all time.} \tag{2.10}$$

For a propellant loading which is a function of z we obtain the statement

$$m^* = m_0^* + \int_0^{t^*} \rho^* f(z^*)\; v_z^*\, dt^*, \tag{2.11}$$

where $m_0^* = m_0/m_{\rm bit}$ and $\rho^* = \rho_0 z_0/m_{\rm bit}$.

If we write Eqs. (2.1), (2.5), (2.7) and (2.11) in terms of the dimensionless variables and in differential form, we obtain

$$\frac{dI_1^*}{dt^*} = \frac{L^*V^* + (M^*I_1^* + I_2^*)(dM^*/dt^*) - I_2^*M^*L^*\psi_2 - I_1^*L^*\psi_1}{(L^*+1) - (M^*)^2} \tag{2.12a}$$

$$\frac{dI_2^*}{dt^*} = M^*\frac{dI_1^*}{dt^*} + I_1^*\frac{dM^*}{dt^*} - I_2^*L^*\psi_2, \tag{2.12b}$$

$$\frac{dV^*}{dt^*} = -I_1^*, \tag{2.12c}$$

$$\frac{dM^*}{dt^*} = -\frac{1}{2}\exp\left(-\frac{z^*}{2}\right)v_z^*, \tag{2.12d}$$

$$\frac{dz^*}{dt^*} = v_z^*, \tag{2.12e}$$

$$\frac{dv_z^*}{dt^*} = \left[\alpha\left(I_1^*\right)^2\exp\left(-z^*\right) - \rho^* f\left(z^*\right)\left(v_z^*\right)^2\right]/m^*, \tag{2.12f}$$

$$\frac{dm^*}{dt^*} = \rho^* f\left(z^*\right)v_z^*. \tag{2.12g}$$

The relevant scaling parameters which emerge from the system of equations are defined as:

$$\begin{aligned} L^* &= \frac{L_0}{L_C}, & \psi_1 &= R_e\sqrt{\frac{C}{L_0}}, \\ \psi_2 &= R_p\sqrt{\frac{C}{L_0}}, & \alpha &= \frac{C^2V_0^2L_C}{2\,m_{\rm bit}\,z_0^2}. \end{aligned} \tag{2.13}$$

The initial eonditions for the set of nondimensional differential equations are:

$$\begin{aligned} I_1^*(0) &= 0, & I_2^*(0) &= 0, \\ V^*(0) &= 1, & M^*(0) &= 1, \\ z^*(0) &= 0, & v_z^*(0) &= 0, \\ m^*(0) &= \frac{m_0}{m_{\rm bit}}. \end{aligned}$$

Note that when the propellant is loaded like a slug, the right hand side of Eq. (2.12g) and the second term on the right hand side of Eq. (2.12f) disappear ($\rho^* = 0$).

2.3 Interpretation of the Scaling Parameters

2.3.1 Inductance Ratio: L^*

It is well known that the efficiency of a pulsed electromagnetic accelerator cannot exceed the fractional change of inductance, $\Delta L/L_0$ (see Ref. [4]). This ratio is a measure of the fraction of energy that ean be deposited into eleetromagnetic acceleration of the gas. From Eq. (2.3) we notice that L_C is equal to the total induetanee ehange

available to the accelerator (i.e. $L_C = \Delta L$). Recognizing this allows us to write $(L^*)^{-1} = \Delta L/L_0$. As such, we expect the value of L^* to be less than unity in an efficient pulsed inductive accelerator.

2.3.2 Critical Resistance Ratios: ψ_1 and ψ_2

The ratios ψ_1 and ψ_2 are similar in form to the critical resistance ratio found in the gas-fed PPT literature[20]. Like that ratio, ψ_1 and ψ_2 appear in the circuit equations and control the nature of the current waveforms.

To determine the physical meanings of ψ_1 and ψ_2, we attempt to find limiting solutions to Eqs. (2.12a)-(2.12c). Decoupling the current sheet dynamics (i.e. the acceleration and sheet motion) from the problem allows us to apply the following conditions:

$$\frac{dM^*}{dt^*} = 0, \quad M^* = 1,$$

which dramatically simplify the circuit equations. Under these assumptions the circuit equations can be rewritten as:

$$\begin{aligned} \frac{d^2 {I_1^*}^2}{dt^*} + (\psi_1 + \psi_2)\frac{dI_1^*}{dt^*} + I_1^* &= \psi_2^2\, L^*\, I_2^*, \\ \frac{dI_1^*}{dt^*} - \frac{dI_2^*}{dt^*} &= \psi_2\, L^*\, I_2^*. \end{aligned} \tag{2.14}$$

If the right hand side of first equation is small (≈ 0), then the solution for I_1 is

$$I_1^* = A_0\, \exp\left(-\Psi t^*\right)\, \sin\left(\left(1-\Psi^2\right)^{1/2}\, t^*\right),$$

where we have introduced the new dimensionless parameter $\Psi \equiv (\psi_1 + \psi_2)/2$. The solution is underdamped (ringing) for $\Psi < 1$, critically damped for $\Psi = 1$, and overdamped for $\Psi > 1$. If the right hand side in the second of Eqs. (2.14) is also small, then the induced current in the plasma mirrors the current in the coil:

$$I_2^* = I_1^*.$$

The fact that the current waveform depends on the sum of ψ_1 and ψ_2 implies that within a portion of the (ψ_1, ψ_2) parameter space, contours of constant performance should generally follow the contours given by the equation

$$(\psi_1 + \psi_2)/2 = \text{constant}.$$

To neglect the non-linearities present in the circuit equations and arrive at the limiting solutions given above, the values of L^* and ψ_2 must be such that

$$\begin{aligned} \psi_2^2\, L^* &\ll 1, \\ \psi_2\, L^* &\ll 1. \end{aligned}$$

Therefore, we expect a feature or transition in the accelerator performance as either $\psi_2^2\, L^*$ or $\psi_2\, L^*$ approaches unity.

2.3.3 Dynamic Impedance Parameter: α

The parameter α is similar to the one found in the PPT literature[4, 20]. Following Jahn[4], we can write α as the product of several important ratios:

$$\begin{aligned} \alpha = \frac{C^2 V_0^2 L_C}{2 m_{\text{bit}} z_0^2} &= \frac{1}{2} \frac{C V_0^2/2}{m_{\text{bit}} v_z^2/2} \psi_1 \psi_2 L^* \left(\frac{\dot{L}}{\sqrt{R_e R_p}} \right)^2, \\ &= \frac{1}{8\pi^2} \frac{C V_0^2/2}{m_{\text{bit}} v_z^2/2} L^* \left(\frac{2\pi\sqrt{L_0 C}}{L_0/\dot{L}} \right)^2, \end{aligned} \tag{2.15}$$

where $\dot{L}$ is the dynamic impedance which is defined as $v_z L'$ and L' is defined as an effective inductance per unit length equal to L_C/z_0. The ratios written on the right hand side of the first line are identified as:

- The ratio of the initial stored energy to the plasma kinetic energy, which is also the inverse of thrust efficiency. This term will always be greater than one.
- The critical resistance ratios, ψ_1 and ψ_2, which will both be less than one in a real pulsed electromagnetic accelerator.
- The inductance ratio, L^*, which will typically be less than one in an efficient electromagnetic accelerator.
- The ratio of the dynamic impedance to an average resistance, $\dot{L}/\sqrt{R_e R_p}$. This is a measure of the relative magnitudes of electromagnetic acceleration and Ohmic heating. The square of this term should be much greater than one for efficient electromagnetic acceleration.

In addition, the right hand side of the second line contains:

- The ratio of the resonant period of the unloaded circuit, $2\pi\sqrt{L_0 C}$, to the time it takes for the circuit to increase its inductance by L_0, which is equal to $L_0/\dot{L}$.

The term $L_0/\dot{L}$ identified in the final bullet point above is essentially the timescale on which the current sheet remains in the acceleration region before decoupling from the coil (i.e. residence time). The other term, $2\pi\sqrt{L_0 C}$, is the timescale on which the external circuit naturally operates. When the ratio of the circuit timescale to the residence time is small ($\ll 1$), the external circuit attempts to transfer its energy faster than the current sheet can accept it, leading to an inefficient acceleration process. On the other hand, when the ratio of the timescales is large ($\gg 1$), the sheet moves away from the acceleration coil quickly, exiting the acceleration region and decoupling before the external circuit can transfer the maximum amount of energy to the sheet. Between these two cases exists an optimum value of α where the current sheet's residence timescale is matched to the external circuit, allowing for optimum transfer of stored electrical energy into directed kinetic energy.

2.4 Nondimensional Solutions

2.4.1 Solution Strategy

The set of coupled first-order ODEs given in Eqs. (2.12) can be solved numerically once the mass distribution and the set of scaling parameters given in Eqs. (2.13) are specified. The performance metrics chosen for this study are the exhaust velocity, v_z^*, and the thrust efficiency, which is written in terms of nondimensional parameters as

$$\eta_t = \frac{m^* v_z^*}{2L^* \alpha}.$$

In solving any set of first-order (in time) differential equations, it is important to know when the time histories of the computed variables (specifically v_z^* in our case) should be queried to calculate performance. This question is, in fact, critical to the evaluation of these accelerators. For our non-dimensional model, the integration period will end when one of the two following conditions is reached:

1. The end of the first half-cycle of the accelerator coil discharge is reached and the current I_1^* reverses in sign. When the accelerator current goes through zero, it is going though a point of high dI_1/dt. While the acceleration model doesn't incorporate any ionization physics, it is well known that a new current sheet can form at the face of the coil, causing what is known as a "crowbar discharge". If this occurs, the initial current sheet ceases to undergo acceleration.

2. The sheet travels three characteristic lengths, $z^* = 3$. The sheet couples to the accelerator coil and transfers momentum through the time-varying inductance which is a function of axial separation between the current sheet and the accelerator coil. The inductance asymptotes at $z^* = \infty$ to a finite value as given in Eq. (2.3). The separation distance $z^* = 3$ is chosen as our cutoff for electromagnetic coupling as it represents an inductance change in the circuit of 95% of the coil inductance. Also, the circuit inductance is changing quite slowly for values of $z^* > 3$. We note here that if the calculation is terminated for values of $z^* < 3$ then the accelerator performance is lower while the performance is unchanged if the calculation is terminated at $z^* > 3$.

If the propellant is not loaded like as a slug mass, more effort may be required to include propellant utilization inefficiencies in the total thrust efficiency. To do this, the velocity must be allowed to continue to evolve until all the available mass is entrained by the sheet. However, it should be clear from the above conditions that the calculation may halt before this occurs. If this is the case, the unentrained mass represents a mass utilization inefficiency in the acceleration scheme and the final values of v_z^* and m^* must be corrected to reflect this fact.

The correction begins by realizing that once the sheet is "decoupled", there is no mechanism by which it can transfer impulse to the thruster. However, we shall assume that the sheet continues to entrain the mass it encounters. When the computation is halted, the current sheet has entrained an amount of mass equal to m_f^* and moves at a velocity equal to $(v_z^*)_f$, where the subscript f is used to indicate that these values are

the final data points obtained from the numerical solution. The total mass available to the sheet is $m^*_{\rm bit}$. Conservation of linear momentum is used to compute the corrected sheet velocity as

$$v_z^* = \frac{m_f^*}{m_{\rm bit}^*} \left(v_z^*\right)_f. \tag{2.16}$$

2.4.2 Solutions

We present contour plots of computed performance (v_z^* and η_t) found by solving the nondimensional governing equations while varying the values of the various similarity parameters. The results are presented primarily for a slug mass loading ($\rho_A = 0$). The slug mass loading, while not physically realizable in a gas-fed system, allows for the exploration of the parameter space while minimizing the effects of the mass distribution on the acceleration scheme. The results from the slug mass loading are compared to a uniform fill (ρ_A = constant for z^* between zero and three) and a triangular mass distribution equivalent to that found in the PIT[6] and given by

$$\rho_A = \begin{cases} \rho_0 \left(1 - z/\delta_m\right) & z \le \delta_m \\ 0 & z > \delta_m \end{cases}$$

In all data sets, the baseline values of the nondimensional parameters are $L^* = 0.121$, $\psi_1 = 0.05$, $\psi_2 = 0.13$ and $\alpha = 2.1$. These values roughly correspond to those found in the PIT MkV accelerator[6].

Contour plots of computed efficiency and nondimensional exhaust velocity are presented for varying values of α and ψ_1 (Fig. 2.2A-B), α and ψ_2 (Fig. 2.2C-D), ψ_1 and ψ_2 (Fig. 2.3A-B), and ψ_2 and L^* (Fig. 2.3C-D). We observe several important trends in these data.

First, in Figs. 2.2A,C, we see that the efficiency possesses a local maximum with respect to α. Also, Figs. 2.2B,D show increasing sheet velocity with increasing α, implying a decrease in the residence timescale of the current sheet in the acceleration region. These observations are consistent with our interpretation of α as a dynamic impedance matching parameter.

Efficiency and exhaust velocity increase with decreasing ψ_1 and ψ_2 (Figs. 2.3A-B). This trend will be discussed in more detail in the next section. In addition, efficiency also increases with decreasing L^* showing the importance of increasing the ratio L_C/L_0 in a pulsed electromagnetic accelerator.

In Figs. 2.2C-D and 2.3A-B, we observe a transition point in the solution near $\psi_2 = 3$. This transition is marked by a dashed line in the plots. Similarly, a transition in the solution form is marked by a dashed line in Figs. 2.3C-D. In Sect. 2.3 we discussed the physical meanings and interrelationships between ψ_1, ψ_2 and L^* by linearizing the circuit equations and finding solutions to a limiting case. We found that this linearization held when $\psi_2^2 L^* \ll 1$ and $\psi_2 L^* \ll 1$. For the present value of L^*, the more stringent requirement is the former. In Figs. 2.2C-D and 2.3A-D, a dashed line given by the equation $\psi_2^2 L^* = 1$ is plotted. As the values of either ψ_2 or L^* increase, the non-linear interactions between I_1 and I_2 increasingly affect the solution causing the time-history of I_2 to increasingly deviate from that of I_1. The same

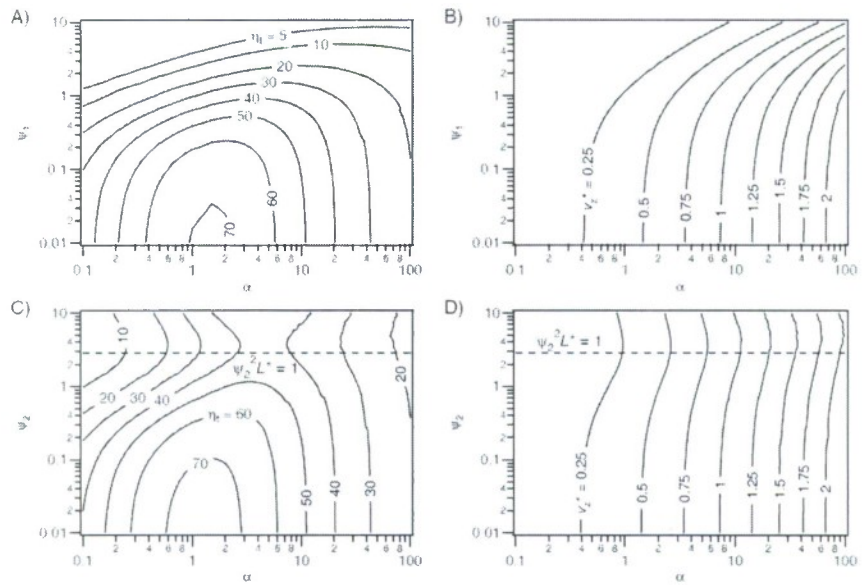

Figure 2.2: Contour plots of inductive accelerator efficiency and non-dimensional exhaust velocity for a slug mass loading found while varying: A) and B) α and ψ_1, C) and D) α and ψ_2. The other nondimensional values use to compute these data are: plots A) and B) $\psi_2 = 0.13$, $L^* = 0.121$; plots C) and D) $\psi_1 = 0.05$, $L^* = 0.121$.

analysis showed that the quantity $\Psi = (\psi_1 + \psi_2)/2$ was important in determining the oscillatory nature of the current waveforms. We speculated that so long as the linearizing assumptions held, contours of constant performance should follow contours of Ψ equal to a constant. In general, we observe this to be true in the lower left hand corners of Figs. 2.3A-B.

We observe that propellant loading has a large influence on the thrust efficiency, going from a maximum of 70% for a slug mass (Fig. 2.2A) to 50% for a triangular mass loading (Fig. 2.4A) and 16% for a uniform fill (Fig. 2.4B). These extreme cases help emphasize the detrimental effects of drag on the current sheet as it entrains propellant. The performance is especially poor in the uniform fill case since much of the propellant is acquired after the circuit experiences a significant increase in inductance. Consequently, a current sheet with substantial velocity but little momentum propagates into the remaining propellant and experiences significant drag (drag force $\propto (v_z^*)^2$) while at the same time the driving force is decreasing exponentially with increasing axial position.

It is interesting to note that there is only a small amount of variation in the peak efficiency as a function of α when comparing Figs. 2.2A and 2.4. The peak slowly shifts from α between 1 and 2 for a slug mass loading to between 2 and 3 for the

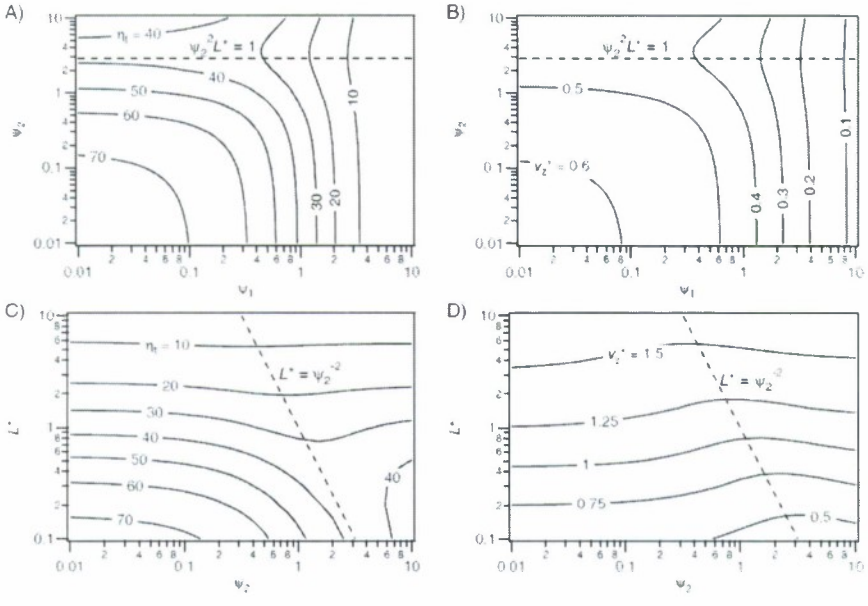

Figure 2.3: Contour plots of inductive accelerator efficiency and non-dimensional exhaust velocity for a slug mass loading found while varying: A) and B) ψ_1 and ψ_2, C) and D) ψ_2 and L^*. The other nondimensional values use to compute these data are: plots A) and B) $\alpha = 2.1$, $L^* = 0.121$; plots C) and D) $\alpha = 2.1$ and $\psi_1 = 0.05$.

uniform fill. The corresponding nondimensional parameters for PIT MkV data are plotted as "+" symbols in Fig. 2.4A and the measured thrust efficiencies associated with these points compare quite favorably with the computed performance contours in that graph. These data also show that the optimum α values are easily accessible experimentally.

2.5 Implications of the Results

Several observations made in the previous section lead directly to ways in which the performance of a pulsed inductive accelerator can be improved. First, an accelerator can achieve maximum efficiency when operated at or near values of α which allow for a good dynamic impedance match. According to the discussion in Sect. 2.3, this match occurs somewhere between $\alpha \ll 1$ and $\alpha \gg 1$. Subsequently, it was shown in Figs. 2.2A and 2.4 that the optimum in fact occurs when $1 \leq \alpha \leq 3$.

The value of L^* should be as low as possible to allow for as much electromagnetic acceleration as possible. In addition, the exhaust velocity can be increased by increasing the value of α.

The scaling with ψ_1 and ψ_2 is somewhat counterintuitive based on previous expe-

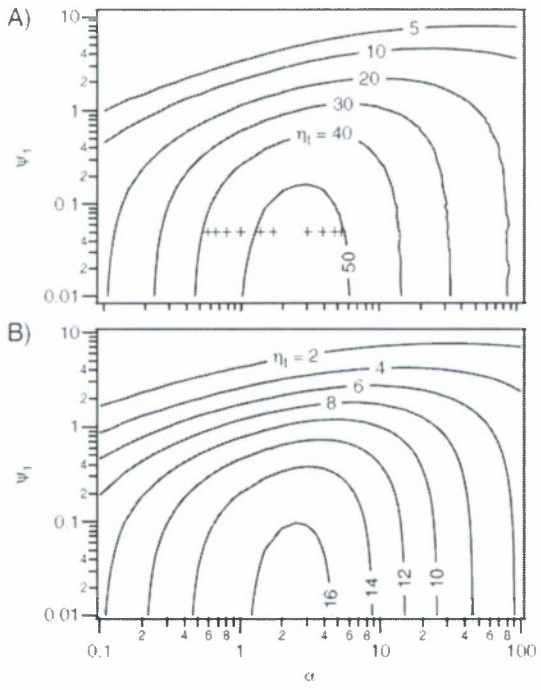

Figure 2.4: Contour plots of inductive accelerator efficiency for A) a triangular mass distribution and B) a uniform mass distribution. The fixed nondimensional parameters in these computations are $\psi_2 = 0.13$, $L^* = 0.121$. Points corresponding to the nondimensional parameters found in the PIT MkV[6] are plotted in A) and are indicated by "+" symbols. The measured thrust efficiencies associated with these points compare quite favorably with the computed performance contours.

rience with pulsed plasma thrusters[21]. In PPTs the thrust efficiency decreases as a function of an increasing critical resistance ratio, which is similar to what we observe in Figs. 2.2A,C and 2.3A. However, unlike the trends in PPT scaling where the thruster exhaust velocity decreases with decreasing ψ[21], the dimensionless exhaust velocity remains fairly constant as either ψ_1 or ψ_2 are varied independent of each other (Figs. 2.2B,D). This is because the term that really matters as far as controlling the discharge waveform is Ψ (see Sect. 2.3.2). In addition, the dimensionless exhaust velocity actually *increases* as *both* ψ_1 and ψ_2 (or Ψ) decrease in value (Fig. 2.3B). Based on this scaling we must ask ourselves if we should attempt to operate a real pulsed inductive accelerator in the low ψ_1, ψ_2 regime.

Plotted in Fig. 2.5 are computed time histories of the various nondimensional parameters. To generate these curves, the equation set was integrated for different values of $\psi_1 = \psi_2$ while maintaining α and L^* constant. We observe two features in these

data. The first is that the current waveforms do ring more as the values of ψ_1 and ψ_2 are decreased. This is evidenced in both the peak currents reached (both I_1^* and I_2^*) and the amount of voltage reversal after the first half-cycle and is an expected result based upon the analysis which yielded Eq. (2.15) and the dimensionless parameter Ψ. However, even though the circuit rings more (i.e. more energy returns to the capacitor at the end of the first half-cycle) the directed kinetic energy of the sheet and the thrust efficiency also increase as ψ_1 and ψ_2 decrease.

To explain this, we first note that α is invariant in these solution sets. Taking the interpretation of α as the dynamic impedence allows us to state in rough terms that the source (driving circuit) and the load (current sheet) are still roughly matched in all three cases plotted in Fig. 2.5. Consequently, we still obtain a high degree of energy transfer between the circuit and the load, even as ψ_1 and ψ_2 are decreased in value. This is why the solutions for the three cases, especially those for I_1 and I_2, while differing in magnitude, qualitatively behave in a similar fashion.

To explain the increase in exhaust velocity and thrust efficiency with decreasing ψ_1 and ψ_2, we first recall that in pulsed plasma thrusters

$$\text{Impulse Bit} \sim \int I^2 \, dt.$$

As the PPT circuit is adjusted from underdamped to critically damped, the peak current decreases. However, the total integral, and hence the impulse bit to some extent the thrust efficiency, can be conserved. On the other hand, in a pulsed inductive accelerator

$$\text{Impulse Bit} \sim \int I_1^2 \, e^{-z(t)} \, dt.$$

This indicates that to improve impulse bits and thrust efficiencies, the current must peak while the sheet is still close to the back-end of the accelerator (i.e. near $z = 0$). The force accelerating the sheet drops exponentially as the sheet moves away from $z = 0$, *even if the peak current is maintained.* Therefore, to achieve efficient pulsed inductive acceleration, the highest possible peak current must be reached before the sheet moves far from $z = 0$. This implies that any attempts to lower the peak current and extend the current pulse length (either by increasing ψ_1 and ψ_2 to obtain a critically damped circuit or through the use of solid-state switching technology) will result in a less efficient acceleration process with a higher fraction of the total energy lost in the circuit through resistive dissipation.

There are several reasons why PPTs typically avoid the low critical resistance ratio, highly-underdamped circuit regime. The missions for which PPTs are best suited require high specific impulse, so the exhaust velocity must be high. Also, the highly ringing circuit can result in a large voltage reversal which can be damaging to the lifetime of the capacitor. In addition, ringing circuits can result in crowbar discharges which short-circuit the acceleration process before the current sheet reaches the ends of the electrodes.

In pulsed inductive accelerators, the problem of crowbar discharges can be avoided by maintaining a good dynamic impedance match. High specific impulses and efficiencies are realized in the low ψ_1, ψ_2 circuit configuration. The only remaining concern

pertains to the capacitor voltage reversal. The voltage reversal for the data presented in Fig. 2.5 ranges from 20% of the maximum charge for $\psi_1 = \psi_2 = 1$ to 40% of the maximum charge for $\psi_1 = \psi_2 = 0.1$. It may be possible to reduce this by adjusting the values of L^* and α slightly. This implies that for high performance, a pulsed inductive accelerator should be operated in a highly underdamped mode. This may require the capacitor to handle a higher voltage reversal than in the critically damped mode.

2.6 Conclusions

We have presented a nondimensional acceleration model for a pulsed inductive plasma accelerator. The nondimensionalization of the governing equations led to the identification of several performance scaling parameters, many of which have analogous counterparts from previous pulsed plasma thruster nondimensional acceleration models. The physical meanings of the scaling parameters and their effects on accelerator performance were explored through a series of theoretical arguments and numerical solutions. The analysis leads to the following insights:

- There exists a value of the dynamic impedance parameter, α for which thrust efficiency is maximized. This value is between 1 and 2 for a slug mass loading and 2 and 3 for the uniform fill. This optimum corresponds to a matching of the driving circuit's natural oscillation timescale to the residence timescale of the current sheet in the acceleration zone.

- Efficiency increases for decreasing values of the inductance ratio, L^*, as this represents an increase in the fraction of energy which can be deposited into electromagnetic acceleration of the propellant.

- Efficiency and exhaust velocity increase when both ψ_1 and ψ_2 (or equivalently Ψ) are decreased in value. This implies that underdamped circuits are preferable for increased performance in pulsed inductive accelerators. The reason is due to the scaling of the performance with $\int I_1^2 e^{-z(t)}\, dt$. Consequently, the greater initial currents found in highly underdamped circuits (relative to critically damped circuits operating at the same discharge energy) are preferable for higher performance.

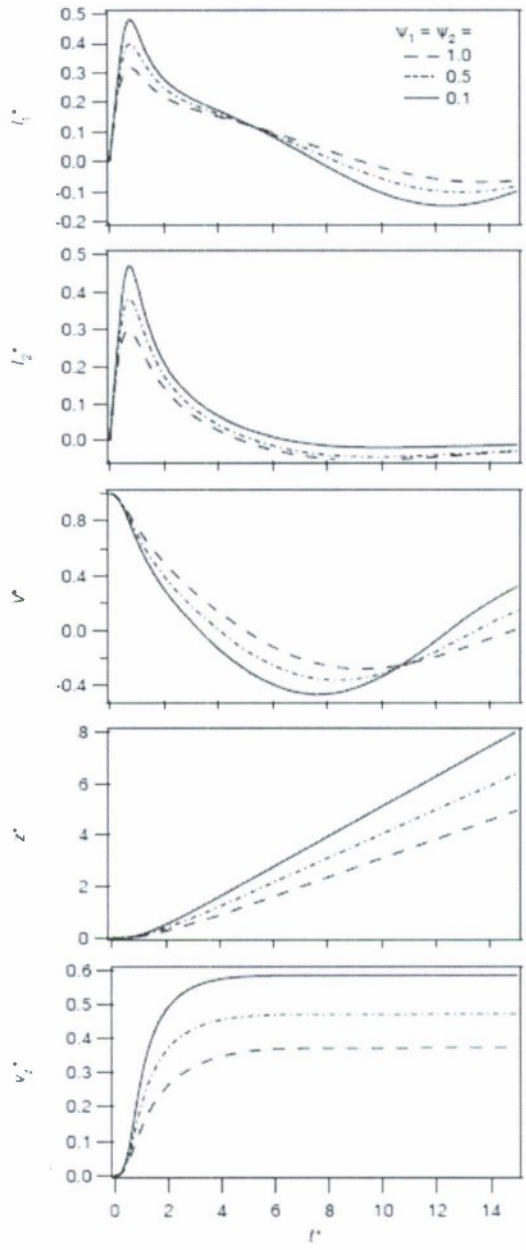

Figure 2.5: Time histories of the various eomputed parameters in a pulsed induetive accelerator for different values of $\psi_1 = \psi_2$. The slug mass loading is employed and the values of α and L^* are 2.1 and 0.121, respeetively.

Chapter 3

Current Sheet Formation in a Conical Theta Pinch FARAD (CTP+FARAD)

3.1 Introduction

The Conical Theta Pinch FARAD (CTP-FARAD) is a permutation of the original FARAD concept with the single difference that a conical inductive coil is used instead of a flat coil. Figure 3.1 shows, in the left panel, a schematic of the original FARAD design with the flat acceleration inductive coil. In the present work, the flat coil is is replaced by the conical coil shown in the right panel of the same figure. This geometry allows for a non-cusp applied magnetic field that more closely follows the coil's face and that should be more effective at guiding the pre-ionized propellant to the coil. Because of this conformity to the natural path of plasma diffusion, current sheets are possible in CTP-FARAD even with no applied magnetic field. Moreover, the CTP-FARAD cone is expected to produce an additional thrust component derived from electromagnetic pinching of the plasma.

The propulsive efficacy of the current sheet depends on a number of factors (e.g., sheet strength, extent, decoupling distance from the coil, propellant leakage, pinching, stability, etc.). Only two of these, namely strength and extent, are the focus of the present study. Specifically, the thruster should ideally induce a strong (high current-density) current sheet that uniformly extends over the entire coil surface in order to maximize the amount of work done on the plasma. An understanding of the mechanisms and conditions controlling the intensity and extent of the current sheet would be useful in providing guidance for future designs and in choosing operating conditions that most enhance these two sheet performance indicies with respect to propulsive efficiency.

The goal of the study reported here is to provide the first clues on the underlying mechanisms and conditions behind the formation, intensity and extent of current sheets

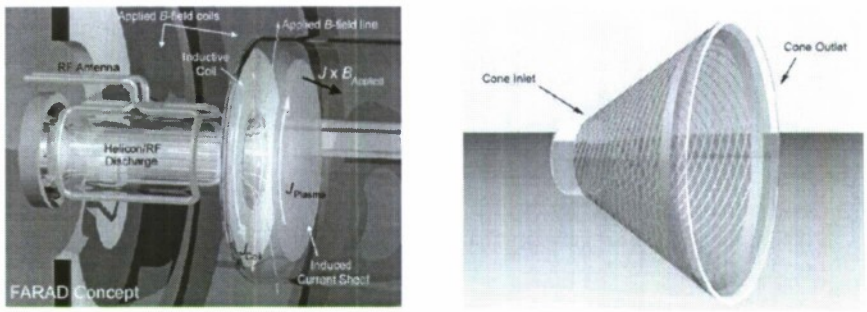

Figure 3.1: *Left:* Schematic of original FARAD set-up with flat Inductive coil. *Right:* Schematic of replacement conical coil.

in CTP-FARAD. Ultimately, for a given physical configuration, we need to know how to maximize the thruster's performance as a function of the controllable operating parameters (mass flow rate, propellant type, RF power, and applied magnetic field topology and strength). In the present study we start with our attempts at elucidating the underlying physical mechanisms by focusing on the most basic dependencies of sheet formation, namely the role of background density. While in a real thruster the background density, for a given configuration and RF power, is controlled by the mass flow rate through the thruster, in this basic study we chose to control the background density by varying the uniform back-fill gas pressure, while holding all controllable parameters fixed and applying no magnetic field. This removes the complications of the flow and expansion the pre-ionized gas from the picture and allows for a clearer isolation of the basic mechanisms controlling current sheet formation, strength and extent.

Furthermore, before carrying out detailed studies using Langmuir probes, B-dot probes, and more analytical optical diagnostics, we limited our initial investigation to a single diagnostic: time-integrated photography. This was motivated by the visually rich character of the distinguishable visible-light emission associated with the sheet.

The rest of the paper is organized into successive sections in which we describe the experiment, document the new conical coil design, describe the photographic data collection, report the observed trends and attempt to extract physical insight into some of the basic mechanisms underlying sheet formation, strength and extent.

3.2 Experimental Setup

3.2.1 Vacuum Chamber

All experiments were performed in a vacuum chamber consisting of two pyrex cylinders joined together by a fiberglass plate on which the CTP is mounted, extending 12 cm into the larger cylinder. The smaller cylinder has an inner diameter of 6 cm and is 37 cm long and the larger cylinder has an inner diameter of 20 cm and is 46 cm long. While the experiment can be operated with mass injection through the endplate

of the smaller cylinder, for the present study the chamber is back-filled to various pressures from a port on the opposite end of the experiment. The pressure is monitored using a Granville Phillips 275 mini-convectron pressure gauge. Plasma is created in the smaller, pre-ionization chamber and diffuses through a 6 cm inner diameter concentric hole in the fiberglass plate into the region bounded by the CTP before eventually migrating into the remainding volume of the larger cylinder. A 150 l/s turbomolecular pump backed by a roughing pump is attached to the larger cylinder at the endplate opposite the CTP inductive coil; the same endplate where gas is fed into the vacuum vessel.

3.2.2 Plasma Source

A Boswell-type saddle antenna is wrapped around the smaller cylinder, creating the pre-ionization chamber. The saddle is composed of quarter-inch copper tubing attached to a water cooling line. An ENI 13.56 MHz 1.2 kW power supply is coupled to the antenna through a tuner consisting of two Jennings 1000 pF 3kV variable vacuum capacitors located immediately next to the antenna and used to minimize reflected power. A Faraday cage surrounds the entire experiment to shield from radiated RF fields.

3.2.3 Conical Theta Pinch

The conical theta pinch is composed of a flexible circuit board wrapped around a pyrex funnel with a wall thickness of 4 mm and providing structural support to the circuit board. The neck of the funnel, with a 6 cm inner diameter and 2 cm length, fits into the concentric hole in the fiberglass plate holding the funnel's axis parallel to the horizontal plane. The conical coil used for the present study has a half-angle of 30 degrees. The design of the circuit board, shown in Fig. 3.2, is based on the design of the flat inductive coil found in the current PIT[22] and the original FARAD experiment. The circuit traces follow an Archimedes spiral with current flowing down one surface from the bus at the major radius to plated through holes at the minor radius. This current then proceeds up the back side of the circuit board (shown as lighter-colored traces in Fig. 3.2), providing cancellation of the radial component of current with the traces from the front side. In this way, the circuit produces a purely azimuthal current that is uniform across the coil face. The traces that form this azimuthal current end 4 cm before the downstream end of the cone, and all normalization made with respect to a particular distance from the cone inlet is made with respect to the downstream end of the cone (not the edge of the inductive coil).

Current is fed to the coil through strip-lines, one between a 39.2μF capacitor and the vacuum vessel and another from the interior wall of the vacuum vessel fiberglass plate to the circuit-board bus (shown in Fig. 3.2). The circuit penetrates the vacuum vessel through metal standoffs, which connect the two striplines. The current pulse is initiated (as in the FARAD) using a "hammer" switch. When a current pulse is thus fed into the coil, a time changing radial and axial magnetic field and an azimuthal electric field are induced in the volume contained by the coil. If pre-ionized propellant is present within the decoupling distance of the coil, a current sheet will be induced in this propellant during the first half-cycle of the pulse at voltages an order of magnitude

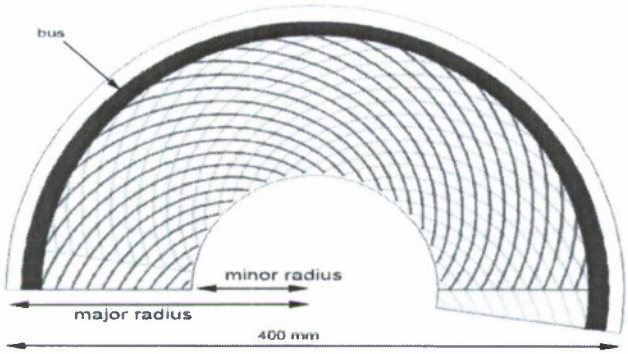

Figure 3.2: The CTP inductive coil shown as it is a print on a circuit board, with twenty spirals per side printed onto a .002 inch-thick Kapton substrate to maintain flexibility. Current is fed to the circuit through the bus, flows down the darker-colored traces on the front side of the circuit board, through plated through holes at the minor radius, and then up the lighter-colored traces on the back side. The ends of the board are brought together to form the conical theta pinch.

lower than those required for operation of the PIT [23]. This current sheet will form such that, inside of the sheet, its own induced field cancels out the magnetic field from the coil and, between the current sheet and coil, the two induced fields add. This build-up of magnetic pressure acts to accelerate the current sheet away from the coil normal to the coil surface for a uniform induced magnetic field profile.

Since the force is normal to the coil surface, the CTP inductive coil provides a radial force density on the plasma current sheet as well as an axial one. The axial component of the force density contributes to the total thrust by imparting axial directed kinetic energy to the current sheet and any entrained propellant. The radial force density component takes advantage of a portion of the pre-ionized propellant that is not involved in current sheet formation by pinching the current sheet, and can provide an additional contribution to thrust as well as reduction in the divergence of the exiting plasma. Schematics showing the idealized stages of sheet formation and pinching are shown in Fig. 3.3.

3.2.4 Time-integrated Photography

A Nikon D50 digital SLR camera with a 50 mm focal length lens was used to capture time-integrated images of the luminous pattern associated with the current sheet. All automatic compensation for light intensity, gamma, and color balance were defeated in the acquisition of these data. Each picture was taken with a half second exposure time, an ISO of 400, and a preset whitebalance of uniform gray. The camera was mounted for a top view of the cone at a distance of roughly 60 cm from the cone exit. Due to physical constraints of the experimental setup, the camera is unable to view the cone surface at an angle where the "film plane" of the camera is parallel to the plane

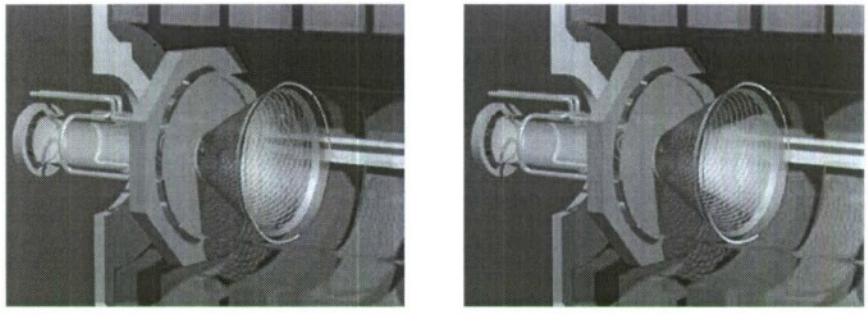

Figure 3.3: Idealized schematics showing current sheet formation (left panel) and pinching (right panel) in the CTP-FARAD.

subtending the bottom edge of the cone. All photographs were obtained with an angle of 30 degrees between these two planes.

The picture frame includes the lower half of the inside cone surface, allowing determination of the intensity and extent of the luminous structure from the cone's inlet to its outlet. The aperture is remotely opened, the switch is then activated sending the current pulse through the coil, and the aperture closes automatically after one half second.

3.3 Experimental Results

3.3.1 Interpretation of the Images

While the steady-state argon discharge from the RF source fills the cone with a gas radiating pink light, this distinct luminosity is greatly overpowered by an azimuthally-symmetric bright blue discharge that emanates from inside of the cone when the switch is closed. We make the assumption that the intensity, location and extent of this latter luminous structure along the wall of the cone are highly related to those of the current sheet. However, previous study of current sheets between plane electrodes[24] using high-speed imaging and B-dot probes showed high correlation between the current carrying structures and their luminous signatures. In our study, the use of time-integrated photography implies a loss of some of this correlation since the luminous structure is more a representation of both the regions where the current has passed at some time during the pulse and those containing radiating gas that does not carry current. Moreover, since the current sheet presumably moves away from the cone's inner surface during the pulse, there is a parallax error associated with determining its location along the cone's surface from time-integrated photographs obtained with a camera whose film plane is not parallel to the cone's axis of symmetry.

Due to these limitations we take the measured intensity, location and extent of the luminous structure that appears during the pulse as rough representations of the corresponding features of the current sheet and limit our conclusions to only relative

changes in these measured quantities.

3.3.2 Image Processing

All image processing is performed in MatLab. The images are filtered for blue light to increase the signal to noise ratio. To further increase the signal to noise ratio, a first photo that includes a current sheet is taken directly before a second photo with no current pulse (but with the background RF plasma on), and this second image is subtracted from the first to eliminate a large fraction of the background light associated with the steady-state RF discharge. This procedure is repeated five times for a given condition and the intensity values are averaged. Intensity values on a line along the cone surface are plotted with respect to distance from the cone inlet. When distance from the cone inlet is normalized, it is normalized to the cone outlet, which occurs at 13.5 cm from the cone inlet. The edge of the inductive coil occurs at 9.5 cm from the cone inlet, and corresponds to a normalized distance of .7. The resulting axial profiles are also integrated and normalized to their peak values to provide a measure of the intensity and extent of the luminous structure.

3.3.3 Measured Profiles and Pressure Dependencies

The RF power source was held constant at 200W forward power and 1% reflected power. No applied magnetic filed was employed and the voltage on the capacitor was maintained at 1.25 kV for each pulse. The argon back-fill pressure in the CTP vacuum vessel was varied from 4 mT up to 48 mT.

Figure 3.4 shows intensity profiles along the cone's wall with the inlet located at 0 cm and the exit at 13.5 cm. Representative profiles from eight back-fill pressure levels spanning the range of varied pressure are shown. The small peak at the latter location is due to light reflection from the downstream edge of the cone.

Figure 3.5 shows the effective intensity of the current sheet plotted as a function of pressure. Effective intensity for a given pressure is calculated by integrating the curve of intensity versus position and normalizing it with respect to the maximum value for that integral attained over the pressure range.

Figure 3.6 shows a plot of effective current sheet extent versus pressure. Effective current sheet extent along the wall (in the axial direction) for a given pressure is calculated as the integral of the curve of intensity versus position divided by the peak intensity for that pressure and normalized to the maximum current sheet extent attained over the pressure range.

The effective location is determined by calculating the centroid for each curve of intensity versus distance from the cone inlet. The centroid locations are normalized by the distance between the cone inlet and exit (13.5 cm), with the cone inlet and beginning of the inductive coil at 0, the inductive coil ending at .7, and the exit at 1, and plotted versus back-fill pressure in Fig. 3.7.

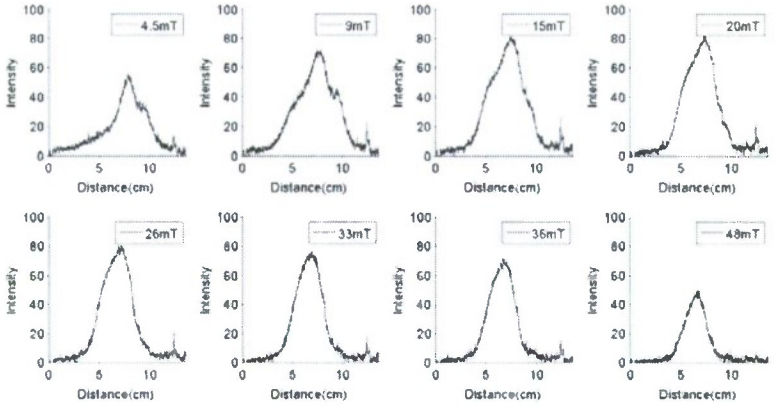

Figure 3.4: Profiles of intensity (in arbitrary units) versus distance from inlet along the cone's wall for eight back-fill pressure levels spanning the back-fill pressure range

3.3.4 Observations

From the experiments and the plots of Figs. 3.4-3.7, we make the following observations:

1. Current sheets of varying intensity, extent and location were observed to form at each of the back-fill pressure levels in the investigated range (4 to 48 mTorr).

2. There is an optimal back-fill pressure, P^* (between 10 and 15 mTorr for the particular conditions of this experiment), for which both the effective intensity and extent of the current sheet are largest (Figs. 3.5 and 3.6).

3. The rate of change in effective intensity (and extent) with pressure differs on either side of this optimal pressure. Specifically, the growth rate of intensity (and extent) with increasing pressure below P^* is significantly higher than its decay rate with increasing pressure above P^*.

4. For pressure levels below P^*, the current sheet intensity profiles are not symmetric and are relatively more extended towards the cone exit. Above P^* they become more symmetric with respect to cone inlet and cone outlet (Fig. 3.4), but at all pressures the current sheet favors the downstream end of the inductive coil.

5. For all pressure levels in the investigate range, current sheet formation occurs around the middle section of the cone but strongly favors the downstream half of the inductive coil. As can be seen in Fig 3.7, current sheet formation occurs at normalized distances of 0.5 to 0.56 from the inlet, while the end of the coil occurs at .7.

6. As the pressure rises the effective location of current sheet formation moves slightly, but definitely and monotonically, towards the inlet (Fig. 3.7).

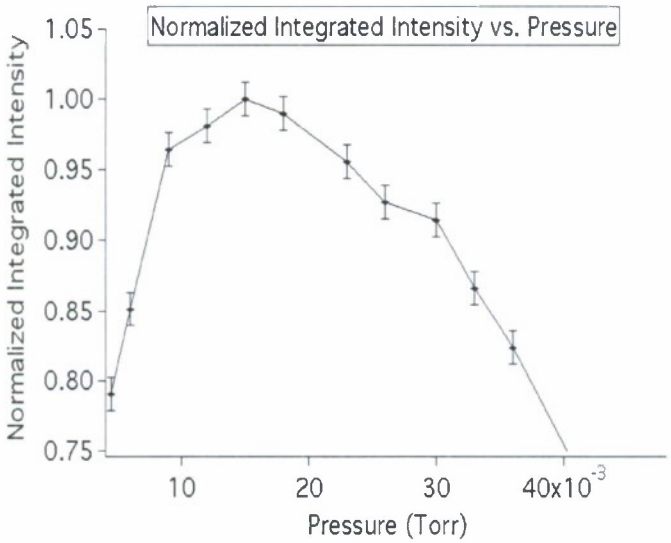

Figure 3.5: Effective intensity of the current sheet as a function of back-fill pressure

We proceed by using these qualitative observations to glean some basic aspects of the mechanisms underlying current sheet formation in such a device.

3.4 Discussion and Interpretation of the Observations

The existence of an optimal pressure (Observation 2) is indicative of a Townsend-like breakdown. On the lower-pressure side of P^*, due to the relatively lower neutral density, the electrons involved in current sheet breakdown undergo fewer ionizing collisions with the background neutrals, while on the higher pressure side of that optimum they gain less energy from the electric field between collisions because their mean free path between collisions with neutrals is smaller.

Unlike in the classic Townsend breakdown, however, there is a finite steady-state background electron density from the steady-state RF discharge in FARAD without which breakdown would require far larger pulse energies. Measurements of a similar RF argon discharge at fixed RF input power of 200 W were reported by Chang et al.[25] and are reproduced in Fig. 3.8. These data show that the electron density *increases* with pressure over the pressure range of our experiment. (Of course this increase cannot go indefinitely at constant power as the energy input per unit mass decreases with increasing pressure.)

The reported increase of electron density with back-fill pressure implies that the decrease in ion production rate due the lower average electron energy on the high-pressure side of P^* is, to some extent, counterbalanced by the increase in the number of background electrons. This would explain the lower rate of decrease in the current

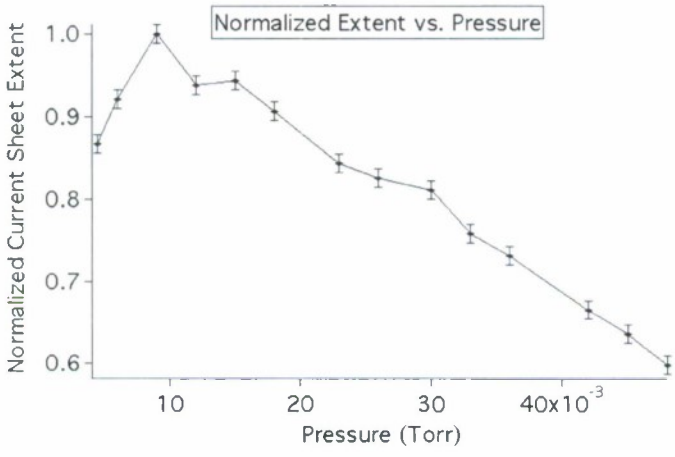

Figure 3.6: Effective axial extent (along the wall) of the current sheet as a function of back-fill pressure. The values of the extent are normalized by the largest value.

sheet's intensity and extent vs pressure at that side of the optimum relative to their increase rate on the lower-pressure side (Observation 3).

It is well know in pulsed plasma thruster research that the current sheet tends to form in such a way that the inductance presented to the circuit is minimized[4]. For the conical theta pinch, this implies a current sheet forming at a location that serves to exclude as much coil-generated magnetic flux from the interior volume of the coil. A current sheet forming at the downstream end of the coil circumscribes a larger area circle than a current sheet forming further upstream. This may explain why the current sheet favors the downstream location.

In addition, a current sheet forming at the downstream edge of the inductive coil will tend to affect magnetic flux lines further upstream, forcing them to stay close to the walls of the theta-pinch to maintain $\nabla \cdot \mathbf{B} = 0$. A current sheet forming near the upstream end, consisting of a smaller ring current, will not have nearly the same effect on the magnetic field lines in the rest of the theta pinch's interior. Consequently, the point of lowest inductance, and the point where the sheet is predisposed to form, is at or near the downstream end of the inductive coil. This may explain why the current sheet has an asymmetric extent favoring the exit end of the coil (Observation 4) and why current sheet formation (at all the investigated pressure levels) is biased (to a varying degree) towards the downstream end of the inductive coil (Observation 5). Because the circuit board traces end 4 cm before the cone outlet, current sheet formation is less dramatically biased toward the exit half of the cone as it is biased towards the downstream edge of the inductive coil.

The remaining observation (Observation 6) that current sheet formation has a tendency to move upstream with increasing pressure may be explained through a consideration of the inductive circuit shown in Fig. 3.9.

The resistivity of a weakly ionized plasma, such as the background RF-produced

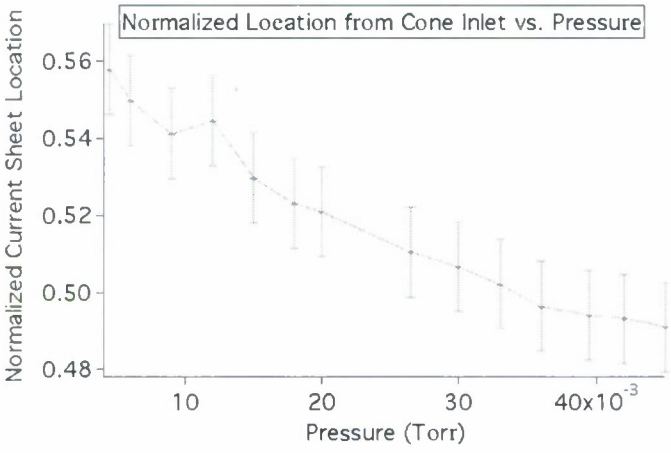

Figure 3.7: Effective location (along the wall) of the current sheet as a function of back-fill pressure. The locations are normalized so that the cone inlet and beginning of the inductive coil are at 0, the end of the inductive coil is at .7, and the cone exit is at 1.

plasma in CTP-FARAD, is dominated by electron-neutral collisions. As the pressure increases, the frequency of these collisions increases, increasing the resistivity in the preionized plasma. During the inductive pulse, the plasma has a resistance R_p that is equal to the resistivity integrated around the circumference of the coil. This value increases for a given axial location as a function of pressure and for a given pressure it decreases as we move axially towards the inlet. From a circuit point-of-view, we recognize that the voltage drop across the transformer must be equal to the voltage drop owing to the plasma resistance. This would require the current sheet to initially form further upstream in the theta-pinch coil as the pressure and R_p increase at a given axial location. Consequently, in a pulsed inductive discharge the sheet may be forced to form at a location other than the point of minimum overal circuit inductance.

3.5 Summary and Concluding Remarks

A photographic study of the effects of back-fill pressure on the intensity, extent and location of current sheets in a conical theta pinch FARAD thruster provide some basic insights into the mechanisms regulating current sheet formation. The existence of an optimal pressure for maximum sheet intensity and strength and the difference in the rates of change in these quantities with changing pressure on either side of this optimum were explained as the behavior of a Townsend-like breakdown modulated by a background electron density that increases with pressure. The effective axial location (along the wall) around which the sheet tends to form, and its dependence on pressure, are thought to be related to a dynamic balance between the resistive elements (depending on plasma resistivity and, thus, pressure) and inductive elements (depending on the

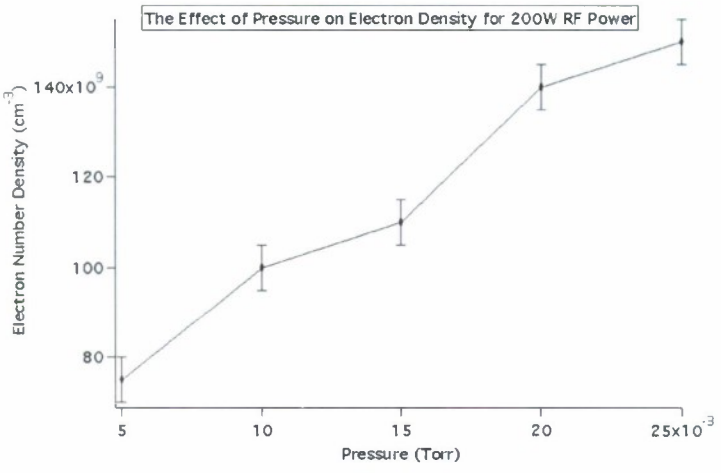

Figure 3.8: The effect of pressure on electron number density in a 13.56 MHz RF inductive discharge.[25]

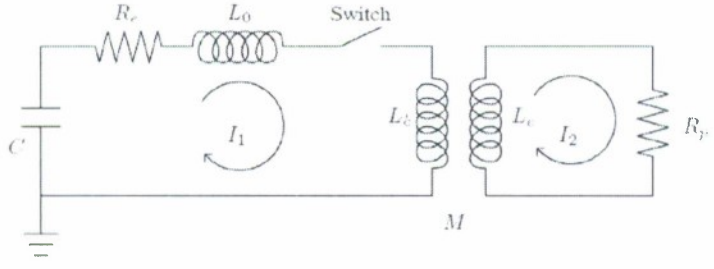

Figure 3.9: Schematic of the inductive circuit used to explain Observation 6

axial location inside the conical coil) of an equivalent inductive circuit.

Future work will aim at verifying and consolidating these insights with more analytical diagnostics and models, with the ultimate goal of deriving prescriptions for optimizing current sheet formation and evolution as a function of controllable operating parameters, including the mass flow rate through the device, applied magnetic field and RF power.

Chapter 4

Design Rules for High-Performance FARAD Thrusters

Designs of pulsed inductive accelerators like the PIT are currently being performed using a set of empirical rules found to work over the years. The purpose of the present work is to state a set of rules and guidelines which can be directly applied to the design of a FARAD thruster. These rules are based upon both the existing set of empirical rules and the results of recent experimental, theoretical and numerical investigations[23] (see previous chapters). Some of the rules apply to pulsed inductive accelerators in general while others are specifically tailored to the FARAD concept and geometry. The sections in the present chapter are organized along the lines of the physical processes present in a FARAD thruster. These are:

- Sect. 4.1: Plasma acceleration,
- Sect. 4.2: Current sheet formation,
- Sect. 4.3: Applied magnetic field generation,
- Sect. 4.4: Mass injection and preionization.

In each section, a set of rules governing the optimization of the design will be outlined. Qualitatively, the rules fall roughly into one of three separate categories, depending upon the level of confidence and theoretical or experimental understanding of the physical processes.

- **Category A**: Rules which are directly supported by experimental results, solid theoretical modeling or knowledge of fundamental plasma physics processes.
- **Category B**: Rules which are supported by a combination of analytical and numerical modeling or are based upon general interpretations of plasma physics scaling relations.

- **Category C**: Rules which are speculative and cannot be proven, or for which some inconclusive or ancillary evidence does exist.

The rules pertaining to the particular physical process are summarized and categorized according to these definitions at the end of each section.

4.1 Plasma Acceleration

A one-dimensional pulsed inductive plasma acceleration model consisting of a set of coupled circuit equations and a one-dimensional momentum equation has been developed by Lovberg and Dailey[6]. In Chapter 2 we nondimensionalized the acceleration model and identified several performance scaling parameters, which we briefly summarize again here.

The dynamic impedance parameter α represents the ratio of the resonant period of the unloaded circuit (i.e. period of the inductive thruster pulse when no plasma is present) to the time it takes for the circuit to double its initial inductance through motion of the plasma sheet. The inductance ratio L^* consists of the ratio of the initial inductance in the circuit to total the inductance change available to the circuit. Physically, L^* represents a measure of the fraction of energy that can be deposited into electromagnetic acceleration. The critical resistance ratios ψ_1 and ψ_2 (or $\Psi \equiv (\psi_1 + \psi_2)/2$) control the oscillatory nature of the current waveforms. The waveforms are underdamped for $\Psi < 1$ and approach critically damped as $\Psi \rightarrow 1$.

The rules governing plasma acceleration are listed below and follow directly from the dimensionless acceleration model studies. The reader is referred to Ref. [4] for greater detail on the compositions and physical meanings of the dimensionless parameters.

- The discharge energy should be increased to raise the specific impulse, I_{sp}, and the impulse bit. This is accomplished by increasing the value of the dynamic impedance parameter α. **(Category A)**

- The Lovberg criteria[?], $\Delta L/L_0 = L^{*-1} > 1$ must be met for efficient electromagnetic acceleration. **(Category A)**

- The propellant depth on the acceleration coil face should be much less than the characteristic electromagnetic coupling distance z_0 to increase the efficiency. Efficiency is maximized for a slug mass loading. **(Category A)**

- If the capacitor can handle higher levels of voltage ringing, the circuit parameters should be optimized such that the circuit is underdamped ($\Psi \equiv (\psi_1 + \psi_2)/2 < 1$) for greater thrust efficiency. **(Category B)**

- Though not universally proven, the maximum thrust efficiency corresponds to $\alpha \approx 2$. **(Category C)**

4.2 Current Sheet Formation

The most important assumption in the acceleration model is that current sheet formation is both immediate (at $t = 0$) and complete (does not allow the induced magnetic field to diffuse through it). This condition has proved most difficult to achieve experimentally. Unfortunately, when current sheet formation is delayed, data show that a significant amount of the magnetic field energy radiates away from the acceleration coil and escapes without performing any useful acceleration.[23]

Current sheet formation occurs more quickly as the accelerator coil current rise rate, dI/dt, is increased[5]. The increasing rise rate leads to the formation of a current sheet that more effectively contains the magnetic pressure radiating from the acceleration coil, leading to a more efficient acceleration process

For a given coil geometry, the simplest way to increase the current rise rate is to increase the ratio of the initial voltage to the initial (parasitic) inductance because the initial current rise rate scales like

$$\frac{dI}{dt} \propto \frac{V_0}{L_0}.$$

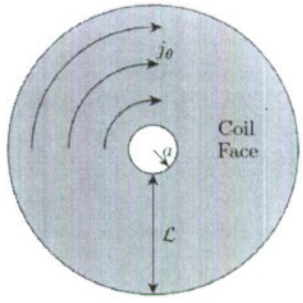

Figure 4.1: Schematic of a pulsed inductive accelerator coil face.

However, we are interested in a general rule that can be applied to a coil of arbitrary size. For this, we need to look not at the total current rise rate in the coil but the linear current density rise rate. If we assume that the linear current density in the coil, j_θ, is radially uniform over the coil face, then for a given coil dimension, $\mathcal{L}$ (see Fig. 4.1), the current density rise rate scales like

$$\frac{dj_\theta}{dt} \propto \frac{V_0}{L_0\,\mathcal{L}}.$$

In the PIT, the value of $V_0/(L_0\,\mathcal{L})$ is approximately equal to 1.5×10^{12} A/(m s). At this value, the current sheet in the PIT forms with little or no delay and is relatively impermeable to the induced magnetic field. The corresponding maximum value of $V_0/(L_0\,\mathcal{L})$ found in the FARAD proof-of-concept experiment was 2.6×10^{11} A/(m s). At this current density rise rate, a current sheet formed in the FARAD, but it did not form very quickly and the experimental data indicate that it was still somewhat porous to both the propellant it encountered and the magnetic field induced by the acceleration coil. This indicates that the rise rate should be further increased in future FARAD designs to levels closer to those found in the PIT to promote faster current sheet formation.

The rules governing current sheet formation in the FARAD are summarized as follows.

- Increasing the current rise rate in the coil leads to faster current sheet formation. For a given geometry, this is accomplished by increasing the ratio V_0/L_0. **(Category A)**

- The linear current density rise rate in the coil, which scales like $V_0/(L_0\,\mathcal{L})$, should have a value approaching 1.5×10^{12} A/(m s). **(Category C)**

4.3 Applied Magnetic Field Generation

Optimization of the applied magnetic field is difficult because it is intimately connected to many of the physical processes in the FARAD, each having its own requirements. The applied field is necessary to generate a helicon plasma. It is also used to guide charged particles from the helicon source to the acceleration stage. Finally, it must not impede current sheet formation and allow for plasma detachment at the end of the acceleration coil pulse. In the present section, we discuss how each of these processes impacts the field optimization problem.

4.3.1 Helicon Source

To support the helicon discharge mode the field must be in the axial direction. We do not wish to delve too deeply into the magnetic field scaling issues associated with the helicon discharge as they are beyond the scope of the study reported in this chapter and are, in fact, the subject of much research (see Refs. [8,9] and the references within). We do wish to note that helicon discharges at low pressures ($p < 5$ mTorr) have been sustained in a 50 G applied field while discharges at higher pressures ($p > 10$ mTorr) typically require field strengths on the order of several hundred gauss[26].

4.3.2 Turning the Plasma

One of the difficulties inherent in the FARAD concept is transporting the propellant from the helicon source to the acceleration coil face. In the original concept[23], it was envisioned that this difficulty could be overcome by exploiting the plasma's natural tendency to follow field lines and employing an appropriately tailored magnetic field topology. This would be accomplished by creating an axial field in the helicon source that transitioned to a radial field and then passed over the face of the acceleration coil.

The strategy of using the magnetic field to turn the plasma is confounded if either: A) the plasma is not fully ionized or B) the ions are not magnetized and do not preferentially follow the field lines. We shall limit our ensuing discussion to two representative cases in an attempt to extract some meaningful design rules and constraints. In the first case we concern ourselves with a partially ionized plasma where the heavy species (ions and neutrals) acts as an unmagnetized fluid while the electrons behave as magnetized particles. In the second case the plasma is fully ionized and both the ions and electrons act as magnetized particles.

Fluid Heavy Species/Magnetized Electrons

The fluid assumption for the heavy species (both ions and neutrals) implies that both are highly collisional and that the ions feel no impetus to preferentially follow the magnetic

field lines. The ion Hall parameter can be used to succinctly state this condition as

$$\Omega_{\mathrm{i}} = \frac{\omega_{\mathrm{ci}}}{\nu_{\mathrm{i}}} < 1,$$

where ω_{ci} is the ion cyclotron frequency and ν_{i} is the total ion collision frequency. Our assumption of magnetized electrons implies that they are not as collisional, allowing us to write the electron Hall parameter as

$$\Omega_{\mathrm{e}} = \frac{\omega_{\mathrm{ce}}}{\nu_{\mathrm{e}}} > 1.$$

However, even if the electron Hall parameter is large, electrons will only follow field lines if their cyclotron radii, r_{ce}, are smaller than the characteristic device length scales at every location in the system. In FARAD, the relevant length scales are: A) the helicon radius, R_H, B) the acceleration stage propellant depth, d, and C) the radius of curvature of the transition between the two stages, R_c (see Fig. 4.2).

The highly mobile electrons are the primary current carriers in the plasma sheet[7]. This implies that the formation of a current sheet at lower discharge energies and voltages is facilitated by the coupling of the free electrons in the preionized plasma to the current pulse in the acceleration coil. Consequently, the applied magnetic field must be designed to deliver electrons from the helicon source to a narrow layer spatially located close to the acceleration coil face.

Two issues arose in the proof-of-concept experiment which impeded the efficient transfer of electrons from the helicon source to the acceleration coil face, both of which are illustrated schematically in Fig. 4.2A. The first was that many of the magnetic field lines intersected with the sidewalls of the containment vessel. This resulted in a reduction of the number of electrons turned towards the coil face and led to a decrease of the preionized plasma density in the acceleration stage. The second problem was that the preionized plasma translated in the axial direction as it was moving radially over the acceleration coil, distributing itself over a wide volume of thickness d in the acceleration stage. Unfortunately, the preionized plasma distributed outside the acceleration region (having length z_0) does not couple with the acceleration coil and is essentially wasted.

A more optimized design which seeks to address the problems listed above is presented in Fig. 4.2B. In this design, the transition between the helicon source and the acceleration stage is contoured such that the sidewalls do not intersect with the magnetic field lines. In addition, our acceleration modeling in Chapter 2 has shown that loading the propellant as a slug mass (i.e. as close as possible to the acceleration coil) results in the greatest thrust efficiency. We cannot turn the heavy species with the magnetic field in this case, but we can use the field topology in the figure to ensure that a dense layer of electrons of thickness $d < z_0$ resides at the coil face. Ideally, the heavy species could be turned by some other means so as to also reside in this layer, resulting in a mass loading approaching a slug mass.

Full Ionization/Magnetized Ions and Electrons

In this case, the electrons can be treated in exactly the same fashion as before. On the other hand, since the ions are also magnetized in this case, they are subjected to the

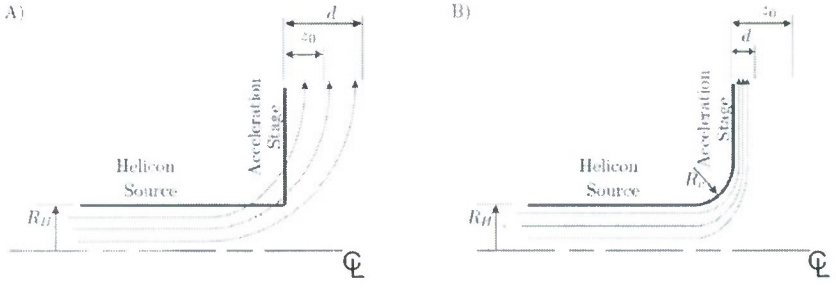

Figure 4.2: A) Schematic of the magnetic field topology in the FARAD proof-of-concept experiment from Ref. [2,3]. B) Optimized magnetic field topology

same conditions and constraints as the electrons. Consequently, the ion Hall parameter must fulfill the inequality

$$\Omega_i > 1$$

and the ion cyclotron radius must satisfy the conditions

$$r_{ci} < R_H,\ R_c,\ d,$$

in each corresponding part of the thruster. If $d < z_0$, the plasma (both electrons and ions) will form a thin layer spatially located very close to the acceleration coil face. Under these conditions, the mass distribution should approach the desired slug mass loading.

As an aside, even if the conditions listed above are fulfilled, the axial field lines located near the centerline of the helicon stage may prove quite difficult to turn. Their tendency is to travel well beyond the acceleration stage before gradually sweeping around and reconnecting back on themselves. Also, the field is weaker at the centerline, making it more difficult to turn any ionized particles located there. This may necessitate the need for a physical nozzle on the centerline to turn the flow.

4.3.3 Sheet Formation and Detachment

As a general rule, the applied field in the acceleration region must not impede the formation of the current sheet and should not affect the acceleration process. In Ref. [12], inductive acceleration modeling resulted in the identification of a dimensionless parameter, γ, which could be recast so as to contain the apparent 'inductance' presented to the circuit by the applied magnetic field. Physically, γ is similar to α in that it represents the ratio of the resonant period of the unloaded circuit (i.e. period of the inductive thruster pulse when no plasma is present) to the time it takes for the circuit to double its initial inductance through motion of the plasma sheet. The difference is that the inductance change in α is attributable to the induced magnetic field while γ

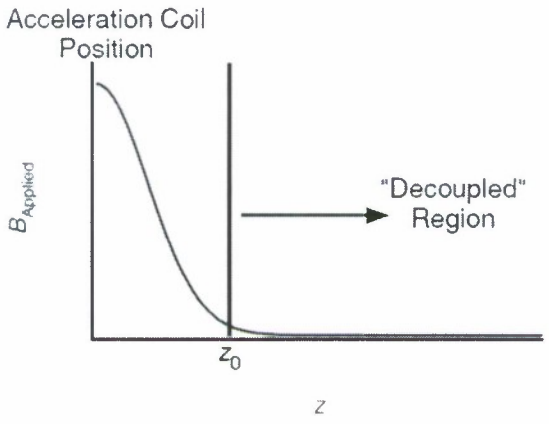

Figure 4.3: Notional graph showing the desired applied field strength as a function of position which will allow for plasma detachment.

takes into account the inductance changes associated with both the induced and applied magnetic fields.

Simulations revealed that the applied field did not have an effect on the acceleration process except in the region of parameter space where $\alpha < \mathcal{O}(1)$ and $\gamma > \mathcal{O}(0.01)$. Physically, this corresponds to operation in a regime where the applied magnetic field strength approaches that of the induced field. It can also be thought of as a region where the inductance presented to the circuit by the applied field approaches the acceleration coil's inductance. This implies that the accelerator should operate in the regime where $\gamma < 0.01$ so the applied field will not affect the motion of the current sheet. This is equivalent to stating that the applied and induced magnetic field strengths should fulfill the inequality

$$B_{\mathrm{r\ Applied}} \ll B_{\mathrm{r\ Induced}}.$$

We know from Sect. 4.2 that added inductance in the circuit slows the current sheet formation process and that this can lead to acceleration inefficiencies. We can assume for the sake of this work that the applied field inductance equally affects the acceleration and current sheet formation processes (which is likely a good assumption since both processes are linear functions of inductance). Consequently, to maintain the current rise rate in the circuit the applied field parameter should not exceed the threshold of $\gamma = 0.01$.

In an efficient acceleration, the current sheet should detach from the applied magnetic field and continue propagating away from the acceleration coil after the current pulse terminates. This will occur if by the end of the pulse the plasma reaches a region of space where the value of the applied magnetic field is small (≈ 0). This implies that the applied field in the acceleration region must possess a maximum value at the coil face and quickly decrease in magnitude as one moves away in the axial direction. The

length scale over which this decrease should occur is the characteristic electromagnetic coupling distance, z_0. This condition can be stated succinctly through the inequality

$$\frac{B_{\mathrm{r\ Applied}}}{|\nabla B_{\mathrm{r\ Applied}}|} \ll z_0,$$

where the gradient is evaluated in the z-direction. A graph showing the notional field strength plotted as a function of position is presented in Fig. 4.3.

Summary of Design Rules for the Applied Field

We can codify the following design rules for a magnetic field which should support a helicon discharge, turn the electrons effectively, and allow the current sheet to escape from the applied magnetic field once the acceleration coil is pulsed.

- The electrons must be magnetized to follow the field lines. Consequently, the conditions $\Omega_e > 1$ and $r_{ce} < R_H,\ R_c,\ d$ must be satisfied everywhere in the device. **(Category A)**
- Thrust efficiency is increased when the current sheet forms very close to the acceleration coil face. Therefore, the depth of the magnetic flux tubes passing over the acceleration coil face (which governs the electron layer depth and sheet initiation location) should be less than the characteristic electromagnetic coupling distance, $d < z_0$, and be spatially located close to the coil face. **(Category A)**
- To reduce plasma losses at the wall of the helicon source, the field topology and the walls of the device should be contoured in such a way that they do not intersect. **(Category A)**
- The applied axial field in the helicon section must be of sufficient strength, $\mathcal{O}(100)$ G, to support the helicon discharge mode. **(Category B)**
- To allow the plasma to effectively cross the applied magnetic field lines, the applied magnetic field strength and the peak induced magnetic field strength should satisfy the criteria $B_{\mathrm{r\ Applied}} \ll B_{\mathrm{r\ Induced}}$. **(Category B)**
- To allow for plasma 'detachment' once the acceleration pulse is complete, the applied field in the acceleration region should conform to the condition

  $$B_{\mathrm{r\ Applied}}/|\nabla B_{\mathrm{r\ Applied}}| \ll z_0.$$

  (Category B)
- To reduce the chance that the field will adversely affect the current sheet formation and acceleration processes, the maximum applied field strength in the acceleration stage should be such that the condition $\gamma < 0.01$ is fulfilled. **(Category C)**

If the plasma is fully ionized and the ions are also turned by the applied field, the following additional conditions must be fulfilled.

- The ions must be magnetized to follow the field lines. Consequently, the conditions $\Omega_i > 1$ and $r_{ci} < R_H$, R_c, d must be satisfied everywhere in the device. **(Category A)**

- The depth of the magnetic flux tubes passing over the acceleration coil face (which governs the ion layer depth and mass distribution) should be less than the characteristic electromagnetic coupling distance, $d < z_0$ and it should also be spatially located near the coil face since thrust efficiency is maximized for a slug mass loading. **(Category A)**

4.4 Mass Injection and Preionization

There are three major pulsed systems in the FARAD (the applied B-field being left in steady-state mode for this discussion). These are the gas valve which introduces the initial propellant pulse into the thruster, the helicon source which preionizes the gas, and the acceleration coil. The pulse length for each system and the intra-pulse sequencing are important from the point of view of mass utilization efficiency and, potentially, total power consumption.

The timing of the different pulsed systems is, in general, very difficult to handle analytically. The thruster's dimensions and the prevailing state of the propellant, be it a partially ionized gas in which only the electrons are magnetized or a fully ionized gas with magnetized ions and electrons, greatly affect the timing. The propellant valve and helicon source have finite response times which must be accounted for when determining the actual switch-on and switch-off times. Also, the convection speed of the propellant through the thruster may change, especially if it is appreciably heated in the helicon source. An additional complication arises if we were to consider that while the propellant pulse is convecting towards the acceleration stage, it is also lengthening through thermal diffusion. Finally, if the ions are magnetized, the changing magnetic field strength, which decreases as the field expands radially in the acceleration stage, may greatly affect the speed at which the ions expand over the acceleration stage face. The ions would experience an increase in velocity parallel to the magnetic field due to conservation of the first adiabatic invariant, μ, defined as

$$\mu = \frac{m v_\perp^2}{2B},$$

where $v_\perp$ is the velocity of an ion in the direction perpendicular to the applied magnetic field.

We should mention that in the case where the heavy species are acting as a fluid, the propellant (ions and neutrals) must somehow be turned so that they propagate radially along the face of the acceleration coil. This could be accomplished using some sort of physical nozzle or duct. However, we must be aware that the object's location in the plasma stream subjects it to constant bombardment and potential erosion. While this technique would turn the flow, the object may become a source of impurities or, even worse, be the life-limiting component in the system.

We see that any attempt to perform an analytical optimization of a FARAD thruster timing scheme would be fraught with considerable difficulties (if it were even analytically tractable). This is really a case in which the timing should be optimized experimentally using fast diagnostics (fast-response pressure gauges and/or Langmuir probes) located throughout the apparatus to monitor the spatial and temporal extent of the gas pulse.

We proceed with a general set of design rules which seek to guide the optimization of the intra-pulse sequencing.

- The neutral gas pulse, of temporal extent Δt_g, precedes the other pulses. The pulse length should be such that the propellant layer which reaches the acceleration stage completely fills the region between the inner and outer coil radii. The amount of additional propellant remaining outside that region constitutes a mass utilization inefficiency since it will not be accelerated when the acceleration circuit is pulsed. **(Category B)**

- The RF pulse length, Δt_{RF}, is the duration that power is supplied to the helicon stage. The RF pulse should not begin until the injected gas has filled the helicon stage. The pulse must remain active long enough to fill the entire acceleration stage with the preionized plasma but be deactivated before producing any extraneous plasma that may not reach the acceleration coil before it is pulsed. **(Category B)**

- The acceleration coil pulse, Δt_a, must not start until most of the preionized plasma has been guided to the back-end of the acceleration stage and completely fills the region between the inner and outer coil radii but it must begin before any significant portion of the leading edge of the preionized plasma begins escaping at the outer edge of the coil. **(Category B)**

- The thruster mass injection system should be spatially compact. This will not only save on thruster mass, but it will allow for a more repeatable mass injection and pulsing scheme by reducing the effects of longer timescale processes, such as thermal diffusion or recombination. The compact construction will most likely lead to an overlap of the neutral gas and RF pulses. **(Category C)**

Before leaving this process, we should mention a few additional caveats which may be employed in a real thruster design. The demand for a fast gas valve can be alleviated by employing a burst-pulse scheme similar to that developed for gas-fed pulsed plasma thrusters[10, 11]. In this mode, a "slow" and sturdy valve is operated at a low duty cycle and the thruster is operated in a burst of discharge pulses. If the response time of the RF-matching network is too slow to switch the preionization pulse on and off for each individual acceleration pulse, it too can operate at the lower duty cycle associated with the "slow" valve. The time between each consecutive *pulse* is equal to the time it takes the current sheet to sweep the gas through the thruster and then refill the acceleration region while the time between the *bursts* is dictated by the available steady-state power and the required (average) thrust. This technique can not only increase the mass utilization efficiency, but by using a more reliable gas valve at a lower repetition rate the lifetime of the thruster can also be extended.

4.5 Summary

We have presented a set of design rules and guidelines aimed at producing an efficient, high-performance thruster based upon the FARAD concept. The discussion was organized along the lines of the various physical processes present in the accelerator, with rules pertaining to a particular process collected in a series of statements at the end of the respective section. The rules are based on a combination of experimental results, analytical and numerical modeling, and physical intuition and we have assigned a qualitative measure of the level of confidence in each specific rule based upon the method of justification employed. A cursory examination of the various rules presented in each section show that some of the rules complement each other. However, further investigation is required to determine whether any of the rules directly conflict with other rules and require a trade-off to optimize the overall thruster performance.

Bibliography

[1] F.F. Chen and R.W. Boswell. "Helicons - The past decade". *IEEE Trans. Plasma Sci.*, **25**(6):1245, Dec. 1997.

[2] R.W. Boswell and F.F. Chen. "Helicons - The early years". *IEEE Trans. Plasma Sci.*, **25**(6):1229, Dec. 1997.

[3] J.A. Lehane and P.C. Thonemann. "An experimental study of helicon wave propagation in gaseous plasma". *Proc. Phys. Soc.*, **85**:301, 1965.

[4] R.G. Jahn. *Physics of Electric Propulsion*. McGraw-Hill Book Company, 1968.

[5] C.L. Dailey and R.H. Lovberg. *PIT clamped discharge evolution*. Technical Report AFOSR-TR-89-0130, TRW Space and Technology Group, Dec. 1988.

[6] C.L. Dailey and R.H. Lovberg. *The PIT MkV pulsed inductive thruster*. Technical Report NASA CR-191155, TRW Systems Group, July 1993.

[7] C.L. Dailey and R.H. Lovberg. "Current sheet structure in an inductive-impulsive plasma accelerator". *AIAA Journal*, **10**(2):125–129, Feb. 1972.

[8] A.R. Ellingboe, R.W. Boswell, J.P. Booth, and N. Sadeghi. "Electron beam pulses produced by helicon-wave excitations". *Phys. Plasmas*, **2**(6):1807, June 1995.

[9] R. Spektor and E.Y. Choueiri. Excitation and propagation of electrostatic ion cyclotron waves in rf-sustained plasmas of interest to propulsion research. In 40^{th} *Joint Propulsion Conference*, Ft. Lauderdale, FL, 2004. AIAA-2004-4095.

[10] J.K. Ziemer, E.A. Cubbin, E.Y. Choueiri, and D. Birx. "Performance characterization of a high efficiency gas-fed pulsed plasma thruster". In 33^{rd} *Joint Propulsion Conference*, Seattle, Washington, July 6-9, 1997. AIAA 97-2925.

[11] J.K. Ziemer, E.Y. Choueiri, and D. Birx. "Trends in performance improvements of a gas-fed pulsed plasma thruster". In 25^{th} *International Electric Propulsion Conference*, Cleveland, OH, 1997. IEPC 97-040.

[12] Wright, E.S. "The design and development of Rogowski coil probes for measurement of current density distribution in a plasma pinch". Report No. 740, Dept. of Aerospace and Mechanical Sciences, Princeton University, Princeton, NJ, June 1965. Also M.S.E. Thesis, May, 1965.

[13] R.H. Lovberg. "Magnetic probes". In R.H. Huddlestone and S.L. Leonard, editors, *Plasma Diagnostic Techniques*, pages 69–112. Academic Press, New York, 1965.

[14] R.H. Lovberg and C.L. Dailey. "Current sheet development in a pulsed inductive thruster". In 25^{th} *Joint Propulsion Conference*, Monterey, CA, July 10-12, 1989. AIAA 89-2266.

[15] T. E. Markusic and E. Y. Choueiri. Photographic, magnetic, and interferometric measurements of current sheet canting in a pulsed electromagnetic accelerator. In 37^{th} *Joint Propulsion Conference*, Salt Lake City, UT, USA, 2001. AIAA-01-3896,.

[16] T.E. Markusic, E. Y. Choueiri, and J.W. Berkery. Measurements of current sheet canting in a pulsed electromagnetic accelerator. *Physics of Plasmas*, 11(10):4847–4858, 2004.

[17] R.H. Lovberg and C.L. Dailey. "Large inductive thruster performance measurement". *AIAA Journal*, **20**(7):971–977, July 1982.

[18] P.G. Mikellides. "Numerical simulations of the pulsed inductive thruster". In *Proceedings of the Space Technologies and International Forum (STAIF) 2003 Conference, edited by M.S. El-Genk*, American Institute of Physics Conference Proceedings, Vol. 654, No. 1, pp. 540-546, January 28, 2003.

[19] P.G. Mikellides. "Numerical simulations of the pulsed inductive thruster". 38th AIAA/ASME/SE/ASEE Joint Propulsion Conference, July 7-10, 2003. AIAA Paper 2002-3807.

[20] Ziemer, J.K. and Choueiri, E.Y. "Scaling laws for electromagnetic pulsed plasma thrusters". *Plasma Sources Science and Technology*, Vol. 10, No. 3, Aug. 2001, pp. 395-405.

[21] J.K. Ziemer. *Performance Scaling of Gas-Fed Pulsed Plasma Thrusters*. PhD thesis, MAE Dept. Princeton University, 2001.

[22] R. H. Lovberg C. L. Dailey. The PIT MkV pulsed inductive thruster. Technical report, Lewis Research Center, 1993.

[23] E. Y. Choueiri and K. A. Polzin. Faraday acceleration with radio-frequency assisted discharge. *Journal of Propulsion and Power*, 22(4):701–710, 2006.

[24] T.E. Markusic and J. W. Berkery E. Y. Choueiri. Visualization of current sheet evolution in a pulsed plasma accelerator. *IEEE Transactions of Plasma Science*, 33(2):528–529, April 2005.

[25] C. Chang, K. Leou, and C. Lin. Real-time control of ion density and ion energy in chlorine inductively coupled plasma etch processing. *Journal of vacuum Science and Technology*, 21(4):1183–1187, July 2003.

[26] K. A. Polzin. *Investigations on the Faraday Accelerator with Radio-frequency Assisted Discharge*. PhD thesis, Princeton University, Princeton, NJ, USA, 2005.